Meteorol. Z. (Contrib. Atm. Sci.), PrePub DOI 10.1127/metz/2019/0982

DACH 2019

Mountain-Associated Waves and their relation to Orographic Gravity Waves

Patrick Hupe[1*], Lars Ceranna[1], Christoph Pilger[1], Alexis Le Pichon[2], Elisabeth Blanc[2] and Markus Rapp[3,4]

[1]BGR, B4.3, Hannover, Germany
[2]CEA, DAM/DIF, Arpajon, France
[3]DLR, IPA, Weßling, Germany
[4]LMU, MIM, Munich, Germany

(Manuscript received June 8, 2019; in revised form September 5, 2019; accepted September 24, 2019)

Abstract

Infrasound covers frequencies of around 10^{-3} Hz to approximately 20 Hz and can propagate in atmospheric waveguides over long distances as a result of low absorption, depending on the state of the atmosphere. Therefore, infrasound is utilized to detect atmospheric explosions. Following the opening of the Comprehensive Nuclear-Test-Ban Treaty for signature in 1996, the International Monitoring System (IMS) was designed to detect explosions with a minimum yield of one kiloton of TNT equivalent worldwide. Currently 51 out of 60 IMS infrasound stations are recording pressure fluctuations of the order of 10^{-3} Pa to 10 Pa. In this study, this unique network is used to characterize infrasound signals of so-called Mountain-Associated Waves (MAWs) on a global scale. MAW frequencies range from 0.01 Hz to 0.1 Hz. Previous observations were constrained to regional networks in America and date back to the 1960s and 1970s. Since then, studies on MAWs have been rare, and the exact source generation mechanism has been poorly investigated. Here, up to 16 years of IMS infrasound data enable the determination of global and seasonal MAW source regions. A cross-bearing method is applied which combines the dominant back-azimuth directions of different stations. For better understanding the MAW generation conditions, the MAW occurrence is compared to tropospheric winds at the determined hotspots. Furthermore, ray-tracing simulations reflect middle atmosphere dynamics for describing monthly propagation characteristics. Both the geographic source regions and the meteorological conditions agree with those of orographic gravity waves (OGWs). A comparison with GW hotspots, derived from satellite data, suggests that MAW source regions match those of OGWs. Discrepancies in the respective source regions result from a stratospheric wind minimum that prevents an upward propagation of OGWs at some hotspots of MAWs. The process of breaking GWs is discussed in terms of the MAW generation.

Keywords: Mountain-Associated Waves, infrasound, orographic waves, gravity waves, atmospheric dynamics, International Monitoring System

1 Introduction

Acoustic waves, including human-audible sound and infrasound, propagate as longitudinal waves through the atmosphere. As opposed to audible sound, infrasound can propagate over thousands of kilometers with low attenuation (Sutherland and Bass, 2004; Evers and Haak, 2010). Consequently, the infrasound technology had already been used to detect nuclear explosions in the atmosphere before the United Nations opened the Comprehensive Nuclear-Test-Ban Treaty (CTBT) for signature in 1996 (Christie and Campus, 2010). The CTBT prohibits any nuclear testing activities, i.e., underground, underwater and in the atmosphere (CTBT Organization, 2019). The International Monitoring System (IMS) was established to monitor compliance with the CTBT. Seismology, hydro-acoustics, and infrasound are the respective IMS waveform technologies used to detect and locate even small explosions with a minimum TNT-equivalent of 1 kt. Complementary radionuclide stations enable the characterization of explosions in terms of a chemical or nuclear nature, the latter of which is a treaty violation.

Acoustic waves travel through the atmosphere at the speed of sound, which is in the adiabatic form written as

$$c_T = \sqrt{\kappa R_s T} \approx 20.05\,\sqrt{T} \quad (\text{in m s}^{-1}), \tag{1.1}$$

with T denoting the absolute temperature (in K), κ is the adiabatic exponent that is well approximated by 1.4, and R_s is the specific gas constant ($R_s = 287\,\mathrm{J\,kg^{-1}\,K^{-1}}$). Winds play another critical role in infrasound propagation. Their effect is best explained using the effective sound speed (e.g., Evers, 2008; Wilson, 2003):

$$v_{\text{eff}} = c_T + w_{\|} \tag{1.2}$$

*Corresponding author: Patrick Hupe, Bundesanstalt fuer Geowissenschaften und Rohstoffe (BGR), Stilleweg 2, 30655 Hannover, Germany, e-mail: patrick.hupe@bgr.de

where $w_{\|}$ is the wind speed parallel to the propagation direction of the signal. This implies that tailwinds increase the effective sound speed, and headwinds reduce it.

In the atmosphere, acoustic waveguides can evolve due to vertical layers of sharp gradients of the effective sound speed. An essential layer in this context is the stratopause region at around 50 km (Drob et al., 2003), where the local temperature maximum and the stratospheric jets can cause strong gradients such that upward-propagating infrasound is refracted downward, according to Snell's Law. As a result of multiple reflection and refraction at the Earth's surface and the stratopause, respectively, and low absorption rates within these altitudes, an infrasound signal can be detected at distances of hundreds to thousands of kilometers from its source. Another potential waveguide, evolving between the surface and the lower thermosphere (approx. 90–120 km), typically limits the detectability of a signal to the first hundreds of kilometers due to high absorption rates in the thermosphere (Drob et al., 2003). At very low frequencies, however, the frequency-dependent absorption is relatively weak (Sutherland and Bass, 2004). For this reason, the atmosphere has been considered to be a low-pass filter (De Groot-Hedlin et al., 2010).

In addition to anthropogenic sources, several infrasound signals of natural origin can be detected in the waveform data, such as volcanoes (e.g., Assink et al., 2014; Matoza and Fee, 2018) or fireballs (e.g., Le Pichon et al., 2013; Pilger et al., 2015). For automatic detection of coherent energy passing an infrasound array, the Progressive Multi-Channel Correlation (PMCC) algorithm was established (Cansi, 1995). In the CTBT context, the PMCC method commonly covers the frequency range between 0.01 to 4 Hz. This study focuses on detections of Mountain-Associated Waves (MAWs), which correspond to lower frequencies of between 0.01 to 0.1 Hz.

First reports on MAWs date back to the 1960s when Cook (1969) observed these waves in North America. According to Campbell and Young (1963), auroral activity was known to produce sound in this frequency range (see also Wilson et al., 2010), but Cook (1969) found, as a result of triangulation, that his observations traced back to mountainous regions (Larson et al., 1971). Therefore, these acoustic waves have been referred to as mountain-associated sound (Chimonas, 1977) or, more commonly, as MAWs (Larson et al., 1971; Rockway et al., 1974; Thomas et al., 1974; Greene and Howard, 1975; Bedard, 1978).

Larson et al. (1971) used data of three sites in the USA – in Alaska, Colorado, and Idaho – and measured amplitudes of 0.05 Pa to 0.7 Pa. They considered local noise to be the reason for the daily variation that they found in the number of detections. Moreover, they proposed a correlation between the seasonal variation in MAW occurrence and cross-mountain wind speeds below the 500 hPa level. Spontaneous sound emission related to atmospheric turbulence (Meecham, 1971) was considered to be a possible cause of MAW generation; however, Larson et al. (1971) supposed a more complex mechanism following Chanaud's (1970) aerodynamic sound theory, suggesting that feedback mechanisms of acoustic energy, such as reflection at the ground, at atmospheric layers, or at surrounding obstacles, could reinforce the sound-producing flow. This would explain the observed duration of MAW events, occasionally lasting for more than 24 h (Larson et al., 1971).

Chimonas (1977) investigated the theory of MAW generation by spontaneous acoustic emissions from vortex shedding due to non-acoustic waves interacting with terrain irregularities. The vortex shedding implies a mechanism similar to the release of the Kármán vortex streets. He used a mathematical, idealized two-dimensional (2D) approach, and concluded that the scattering of wind oscillations to acoustic modes at terrain irregularities could cause "at least part of the infrasound signal" (Chimonas, 1977, p. 806).

Bedard (1978) combined infrasound observations using sensors in the Rocky Mountains (USA) and aircraft observations. The latter was supposed to support the theory of air turbulence being a source of MAW excitation, which was also proposed by Thomas et al. (1974) before. However, Rockway et al. (1974) remarked that the effect of atmospheric conditions on the propagation and detection of MAWs might have been underestimated in previous theories. Their ray-tracing model showed that winds affecting propagation conditions were a vital issue for the seasonality of MAW detections. As a consequence, the knowledge about the propagation conditions is essential to understand the source generation mechanisms.

For the first observations of MAWs beyond North America, a seven-sensors infrasound network, located between Alaska and Argentina, was used. Within one year of measurements, Greene and Howard (1975) found many MAW signals originating between Colorado and Alaska in the Northern Hemisphere and along the southern part of the Andes in the Southern Hemisphere. They noted that the northern part of the Andes exhibited much fewer MAW detections and concluded that the acoustic radiation must depend on topography or combined meteorological and topographic conditions.

Since the late 1970s, however, published studies on MAWs have become rare; for instance, a report on MAWs observed in Japan was given by Nishida et al. (2005). As a consequence, the exact source mechanism has remained unclear. Based on the modeling approach of Chimonas (1977), Chunchuzov (1994) took up again the idea of MAW generation due to wave scattering. He proposed a generation model for non-stationary mountain waves which also allowed the generation of acoustic modes induced by "strong wind gusts among the wind fluctuations near the mountain" (Chunchuzov, 1994, p. 2205). These individual acoustic impulses would propagate in atmospheric waveguides and superpose to the signals that are eventually detected at remote sensors.

Nowadays, the IMS infrasound network provides the opportunity to study MAW signals at remote sites around the globe. Wilson et al. (2010) analyzed MAW detections at IMS stations in Alaska and Antarctica. At each station, they noticed dominant directions of MAW arrivals, especially during winter, each associated with a mountain range or peninsula within hundreds of kilometers from the sensors. Moreover, the detected events exhibited different waveform characteristics. Wilson et al. (2010) argued that more distant mountain ranges resulted in lower frequencies at the sensors than nearer sources. However, without considering additional stations, an exact source localization was not feasible. More recent studies have attempted to provide a global view of infrasound source regions (Blanc et al., 2018; Ceranna et al., 2019), using PMCC detections of the IMS infrasound arrays.

In this study, 16 years of infrasound recordings are considered to create a monthly climatology of MAW detections at all operating IMS infrasound stations. Based on this climatology, a cross-bearing approach is applied to identify the global source regions of MAWs. These steps are described in Section 2. The MAW hotspots and their seasonal variation (Section 3) are investigated using a 2D ray-tracer. Atmospheric input is obtained from the high-resolution (HRES) atmospheric model analysis, provided by the Integrated Forecast System (IFS) of the European Center for Medium-Range Weather Forecasts (ECMWF). In addition to the propagation conditions, the source conditions are analyzed, with a particular interest in tropospheric winds and static stability (Section 3).

Both are essential quantities for another type of atmospheric wave, the gravity wave (GW), and the orographic GW (OGW) in particular. While static stability is a physical prerequisite for the occurrence of GWs, tropospheric winds and the mountain height determine the amplitude, and thus the energy and momentum transport into the stratosphere and mesosphere (Gill, 1982; Holton, 1983). In general, upward-propagating GWs break at altitudes where the waves become unstable; for instance, due to increasing amplitudes (e.g., Nappo, 2012). In this context, a 'critical level' evolves where the background wind equals the horizontal phase speed of the GWs; for stationary OGWs, this is around zero (e.g., Alexander et al., 2010). GW filtering at the critical level results from shrinking of the vertical wavelength, which increases the shear and the dynamic instability, forcing the wave to break (Dörnbrack et al., 1995; Fritts and Alexander, 2003; Nappo, 2012).

Section 4 of this study compares the determined MAW hotspots with satellite-based GW hotspots. The results are discussed in Section 5. This section also addresses the question of whether there might be a link between remote MAW observations and the source mechanism of OGW generation. If so, the IMS infrasound network could enable unique ground-based monitoring of OGW source regions on a global scale using MAW detections. Conclusions are drawn in Section 6.

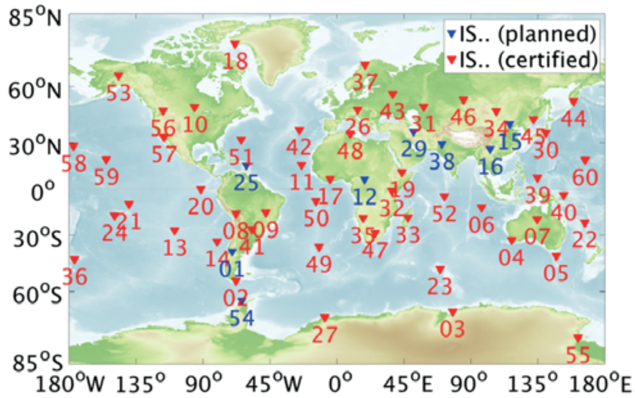

Figure 1: IMS infrasound station map (as of May 2019). Each red triangle represents a certified array, blue triangles depict planned sites, as far as the locations are already known.

Table 1: Applied filtering parameters for studying MAWs with high significance in PMCC detections.

PMCC measures	**minimum**	**maximum**
Family size (group of detections)	10	–
Center frequency of the family [Hz]	0.02	0.05
Frequency of family members [Hz]	0.01	0.07
Apparent phase velocity [m s^{-1}]	300	500
Fisher ratio F	3	–

2 Methodology

2.1 Dataset

When fully established, the IMS network will consist of 60 infrasound arrays (see map in Fig. 1). Differential pressure has been continuously recorded at the IMS infrasound stations for up to 20 years, at a sampling rate of 20 Hz. The detection of infrasound events from these waveform data is performed using the array processing algorithm PMCC (Cansi, 1995). For this study, filters were applied to the PMCC detection lists according to Table 1, to focus on significant detections in the frequency range of MAWs.

Note that the upper-frequency limit was set at 0.07 Hz – instead of 0.1 Hz – to ensure clear discrimination from microbarom detections (0.1–0.5 Hz), a persistent infrasound signal originating from interacting ocean waves (e.g., Donn and Rind, 1972; Hupe et al., 2019). Dominant periods of MAW events have been reported as covering 20 s to 80 s (Larson et al., 1971) or, more narrowly, 20 s to 40 s (Bedard, 1978). Therefore, in addition, the center frequency thresholds were set to 0.02 Hz (50 s) and 0.05 Hz (20 s), respectively. A fundamental prerequisite for detecting MAW signals is low background noise at the recording station (e.g., Matoza et al., 2013), due to the small amplitudes of between 3 mPa and 300 mPa. Fig. 2 shows the residual number of detections per month and station for the IMS infrasound network from January 2003 to July 2017. The color code reflects the respective mean back-azimuths.

Figure 2: The monthly number of PMCC MAW detections is shown for all IMS station datasets available from the German National Data Center (Hupe, 2018). The stations are ordered from north (top) to south; the horizontal black line reflects the equator. The logarithmic scale indicates from 10^0 to 10^4 detections at each station. Colors code the monthly mean back-azimuths; gray boxes indicate missing data or the lack of PMCC results at the time of writing when the data from end-2015 were subject to reprocessing.

A semi-annual pattern was identified at most of the sites. In contrast to the microbarom detections, which clearly correlate with the predominant stratospheric wind directions (e.g., Landès et al., 2014; Ceranna et al., 2019) – i.e., westerly (purple) and easterly (greenish) main back-azimuths – the MAW detections are not simply zonally reversed between summer and winter. Instead, they show meridional components in the back-azimuths. For instance, northern directions (reddish) are pronounced at tropical and subtropical stations in the Northern Hemisphere (i.e., between IS32 near the Equator and IS42 on the Azores), and similarly, both southerly (cyan) and northerly components are found at low latitudes in the Southern Hemisphere (Hupe, 2018).

2.2 Azimuthal distributions of MAW detections

For each station and its period covered, as shown in Fig. 2, a monthly detection climatology in terms of back-azimuth was built (annual average). As an example, the histograms of January, April, July, and October are shown for IS02 (Ushuaia, Argentina) in the Supplements (Figure S1). In general, a maximum of three directional peaks was retrieved from the monthly histograms, reflecting different sources that were potentially detected at a station. The peaks had to fulfill the following conditions (Hupe, 2018):

- The peak was higher than the monthly mean, and there was at least one detection per month.
- The peak had to be 35° distant from other peaks.
- The minimum peak prominence (i.e., the relative peak height from the background detections) was 0.5.
- The minimum peak width at half prominence was 15°.

Referring to the example of IS02, a northwesterly direction (315°, Figure S1 in the Supplements) was consistent and prominent throughout the year. The number of detections revealed a seasonal variability, with a maximum in austral winter and a minimum in summer. A secondary peak at around 170° fulfilled the criteria only in October. The determined peaks were used to apply the cross-bearing approach described below.

2.3 Cross-bearing method for MAW source localization

The PMCC detection bulletins provide information on the detection time, back-azimuth (β), and apparent phase velocity (Cansi, 1995; Le Pichon et al., 2010). The localization of a source, e.g., an explosion in the atmosphere, requires this set of information from at least two different stations. In contrast to explosive events, which appear as transient signals in the waveform data, MAWs are a two-dimensional, ergodic signal, such as ambient noise from microbaroms (e.g., Landès et al., 2012). Therefore, conventional methods based on the onset times of at least two different stations (e.g., Le Pichon et al., 2008) are not applicable to arriving wave trains of MAWs.

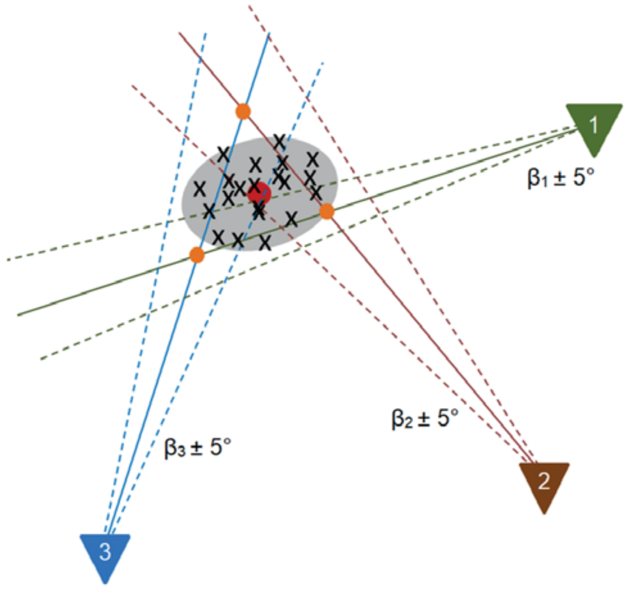

Figure 3: A fictive cross-bearing combination of three stations is shown schematically. Solid lines depict the stations' dominant back-azimuths (β_i), dashed lines represent the ±5° uncertainties. For the main back-azimuths, the intersection points (orange circles) are shown from which the final location (red circle) is derived. For all other combinations, the black crosses mark the final locations. The gray-shaded polygon ultimately highlights the likely source region of a signal detected at all stations.

Here, for each month of the year, the back-azimuths at all IMS infrasound stations were used for a cross-bearing, as described in Hupe (2018). Each determined back-azimuth was attributed a standard deviation of ±5° to account for uncertainties due to the array response or wind conditions along the propagation path (e.g., Le Pichon et al., 2005). This uncertainty results in an azimuthal sector of 10° width. A maximum propagation range of 10,000 km was chosen, in accordance with a similar approach for microbaroms by Landès et al. (2012). This range is assumed to apply to MAWs since atmospheric attenuation is a function of frequency, and the attenuation in these low-frequency domains is generally low (Sutherland and Bass, 2004).

A reliable localization of a signal's origin requires the combination of three stations. For each three-station set out of the IMS infrasound network, all possible combinations of station back-azimuths – i.e., (i) $\beta - 5°$, (ii) β, or (iii) $\beta + 5°$ – were projected along the great-circle paths (one per station). For one three-station set, this amounts to $3^3 = 27$ combinations. Up to three intersection points were calculated for each of these combinations. Fig. 3 demonstrates the procedure schematically.

If three intersection points were found, the back-azimuth projections of all stations in a three-station set intersected. Then the coordinates of this combination's final location were calculated as the longitudinal and latitudinal mean of the intersection points (red circle in Fig. 3). If only two intersection points were calculated, the method could still provide a potential source region, but such localization might be less accurate. Therefore, such results and localizations based on just one intersection point were neglected here.

Another source of uncertainty is a station combination in which at least one pair of back-azimuths points either in the same (one alongside the other) or opposite (towards each other) direction(s). Then slight deviations in the back-azimuths potentially cause significant horizontal shifts in the intersection point coordinates. Therefore, combinations with $\beta_1 - \beta_2 = \pm 10°$ were excluded.

2.4 Ray-tracing for hotspot validation

For associating the infrasound detections with the determined source regions, ray-tracing simulations were carried out using the 2D finite differences (2D-FD) software package of Margrave (2000). This was initially developed for seismological purposes, but it has also been adapted for estimating sound propagation in the atmosphere (e.g., Koch and Pilger, 2018). As an example, the 2D-FD ray-tracer was successfully used for modeling the long-range ducting in case of the low-frequency fireball event of Chelyabinsk (Le Pichon et al., 2013; Pilger et al., 2015).

The ray-tracer calculates infrasound propagation paths based on a 2D effective sound speed field, according to Eq. (1.2). The operational HRES atmospheric analysis from the ECMWF was incorporated in the simulations as a monthly mean, including vertical profiles of temperature, meridional wind, and zonal wind. These were given each 100 km along the great-circle propagation path between the potential source and the receiver. The upper model limit was set to 140 km. Above 78 km altitude, ECMWF data were supplemented by climatological data from empirical models. For the temperature, the Naval Research Laboratory Mass Spectrometer Incoherent Scatter Extended model, NRLMSISE-00 (as of 2000), was used, produced by Picone et al. (2002); winds were obtained from the Horizontal Wind Model, HWM07 (as of 2007), developed by Drob et al. (2008).

It is noted that a sponge layer is implemented in the ECMWF model to suppress uncontrolled wave reflections at the upper model boundary (e.g., Ehard et al., 2016). Vertical temperature profiles observed by lidar instruments have shown the effect of the sponge layer above an altitude of around 45 km, resulting in a cold temperature bias of up to 12 K at 60 km in the ECMWF model (Hupe et al., 2019). However, computations incorporating the mean bias did qualitatively not change the simulation results provided in Section 3.2 (see also Hupe, 2018). The sponge layer will be more relevant when computing single events which can be affected by GW perturbations of the vertical temperature and wind profiles. Moreover, it is noted that the 2D-FD ray-tracer is a high-frequency approximation of the acoustic field; i.e., it is not valid for vertical perturbations with wavelengths smaller than the simulated wavelength (e.g., Le Pichon et al., 2012), which is around 6 km to

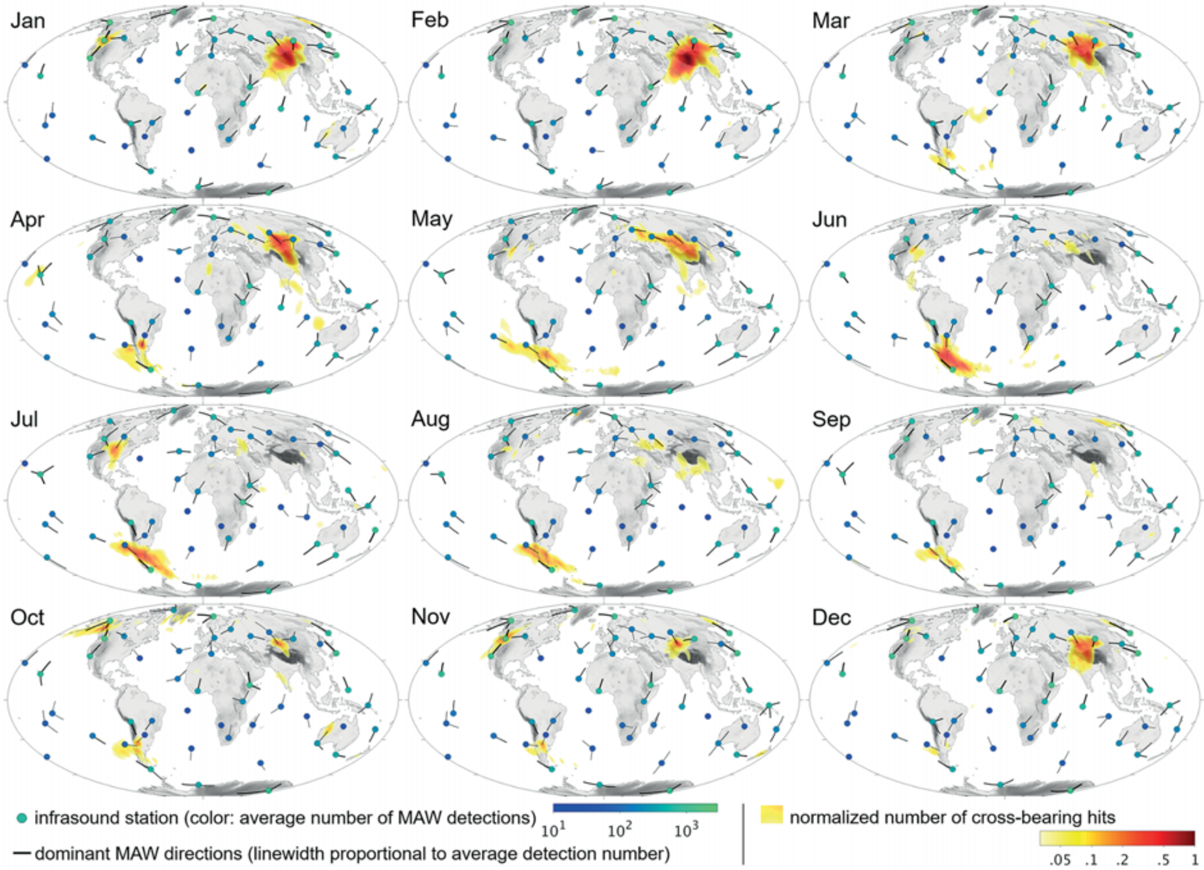

Figure 4: Monthly variation of the global MAW hotspots, based on PMCC detections and the cross-bearing method. The number of localizations per 3° × 3° is normalized by the maximum of all the months. The maximum can be found over the Tibetan Plateau in February. Gray background colors indicate topography, ranging from light ($z < 250$ m) to dark ($z > 7{,}500$ m) gray. Circles depict the IMS infrasound stations (the labels are given in Fig. 1), and the color of each circle indicates the average number of detections during a month. If dominant peaks exist in the azimuthal distribution, these directions are added to the station marker as great-circle lines of equal lengths (10°), whereas the widths are proportional to the corresponding number of detections.

10 km for 0.05 Hz. However, it is assumed to be appropriate when analyzing the monthly mean conditions. For modeling single MAW events with respect to small-scale features of the wave field, the parabolic equation is a more appropriate method (e.g., Lingevitch et al., 2002; Norris et al., 2010).

For the hotspot validation, the stable eigen-ray solutions of the ray-tracer – i.e., the statistically significant occurrence of eigen-rays throughout variations between the source and the receiver – were evaluated. In particular, these solutions, either for ground-to-stratopause or ground-to-thermosphere ducting, were compared with the monthly MAW detections at surrounding stations.

3 Global MAW hotspots and their characteristics

Fig. 4 shows a normalized, monthly view of the cross-bearing results. Four MAW hotspots can be identified throughout the year. The coastal mountain ranges in North America were already identified as a source for MAWs before (see Section 1). The applied method here reproduces these results. Also, the Tibetan Plateau and its surrounding mountain ranges (e.g., the Himalayas) turn out to be a major source region of MAWs on the Northern Hemisphere. Another hotspot is identified in the East Siberian Mountains.

In the Southern Hemisphere, the southern Andes are the major hotspot. A fifth hotspot is the Southern Alps on New Zealand's South Island. The latter is not prominent in Fig. 4 since only a couple of infrasound stations (IS05, IS22, IS36) detect it; however, the MAWs are a dominant feature among these detecting stations. The signals are detected throughout the whole year and trace back to the South Island.

3.1 The seasonal variation in detections

Larson et al. (1971) found an annual cycle of MAW occurrence in North America, with a maximum in the number of detections during the hemispheric winter. Here, the monthly cross-bearing results (Fig. 4) indicate this to be also valid for the most dominant hotspots as discussed below.

3.1.1 Tibetan Plateau

This MAW source region is the strongest, and the cross-bearing results cover a wide area. Many potential sources – i.e., mountain ranges – surround the Tibetan Plateau, including the Himalayas (up to 8,848 m) in the south, the Pamir Mountains (7,649 m) in the west, and the Tian Shan (7,349 m) in the north. The number of detections and cross-bearing hits maximizes in winter. During this season, around ten stations detect MAW signals from this source region, for instance, IS19, IS33, and IS34. In May, the maximum number of cross-bearing hits is only around 10 % of that in winter. The hotspot then disappears in summer; however, two stations – IS31 (Kazakhstan) in the northwest of the hotspot and IS32 (Kenya) in the southwest – detected MAWs during both summer and winter.

3.1.2 North American Pacific coast ranges

This hotspot is located around IS56 from October to January and covers the US Coast Range in Washington (4,392 m) and parts of the Canadian Rockies (3,954 m). The cross-bearing results also highlight the Alaska Range (6,200 m) and the Aleutian Islands (1,900 m) in October. Many mountains within this hotspot are volcanoes. The closest IMS stations – IS53 ($\beta = 128°$), IS56 ($\beta = 325°$), and IS57 ($\beta = 9°$) – detect MAWs originating from this hotspot region until March. From April to July, the number of detections from the southeast (IS53) and north-northwest (IS56, IS57) is reduced by up to 95 %, compared to January (the corresponding histograms are provided in Hupe, 2018). During February and March, the surrounding stations reveal slightly different dominant back-azimuths and the number of detections from far distant stations is reduced. This leads to fewer cross-bearing hits, which is the reason for the disappearance of this hotspot in Fig. 4.

3.1.3 East Siberian Mountains

Over the very eastern part of Siberia (peaks up to 2,000 m), a source region of MAWs is identified from September to March (Fig. 4). It is detected, among others, at IS44, IS45, IS58, and IS59. The detection numbers vary at these stations; the maximum values per month amount to two (IS45, October), four (IS58, October), 20 (IS59, January), and 45 (IS44, January). Although this hotspot is less prominent, compared to the ones above, its seasonal cycle is similar.

3.1.4 Southern Andes

Greene and Howard (1975) had already identified the southern Andes as a source region of MAWs. Their southernmost sensor was located near the highest mountain of the continent (Mount Aconcagua; 41.67° S, 70.00° W, 6,961 m elevation). Here, at least six IMS stations detect MAWs from the southern Andes, and one of these (IS02) operates at the southern tip of the continent. Detections are found almost all around the year, and the latitudinal range of the cross-bearing solutions extends from 30° S to south Chile (55° S), where the mountains (mostly volcanoes) reach elevations of 1,500 m to 2,500 m. Note the broad longitudinal range of cross-bearing hits exceeding the coastlines, which poses the question of whether this is caused by real events or methodological artefacts. MAW detections originating from upstream and downstream of the hotspot could be associated with the phenomenon of trailing GWs, which have been particularly observed in the lee of New Zealand (Ehard et al., 2017; Jiang et al., 2019). The dominant back-azimuths of IS08 detections often match the identified hotspot region downstream of the southern Andes. However, Fig. 4 also indicates different back-azimuths of the other stations, and additional cross-bearing hits are located upstream of the Andes. Therefore, at least some of the cross-bearing results are likely methodological artefacts resulting from the applied uncertainty of ±5° or the possibility that the IMS stations detect different sources within that region – for instance, the closest to each station. The latter issue would cause the triangulation to fail matching any of the detected sources exactly.

Overall, the southern Andes are the most active hotspot of MAWs in the Southern Hemisphere. A seasonal cycle in the number of detections is evident, showing a maximum in winter. The cross-bearing results highlight this hotspot from September to May (Fig. 4). At IS02, however, MAWs are also detected in summer (maximum 17 detections per month), from almost the same direction as in winter (56 detections).

3.1.5 Southern Alps of New Zealand

The azimuthal distributions of detections show prominent peaks related to MAWs at IS05 ($\beta = 100°$), IS22 ($\beta = 165°$), and IS36 ($\beta = 265°$) all year round. At IS22 the spectral number maximizes in July (59), opposed to only three detections in December. At IS36, the seasonal cycle is similar, but the highest peak in May shows just 13 detections. Such differences between the stations can be related to the propagation conditions between the source and the receiver. Section 3.2 investigates the propagation conditions for the hotspots identified in the Southern Hemisphere.

3.1.6 Further results

Further regions that show accumulations of cross-bearing results in Fig. 4 are Greenland (October), northwestern Australia (January, October), and the central USA (May to August). Greenland is a potential source region of MAWs; however, there are not enough stations around for continuous cross-bearing results. Moreover, northwestern Australia is highlighted as a result of spurious intersections, due to the wide range of the cross-bearing approach. The closest stations in Australia – IS04, IS05, and IS07 – do not detect any MAW signals from the appropriate directions.

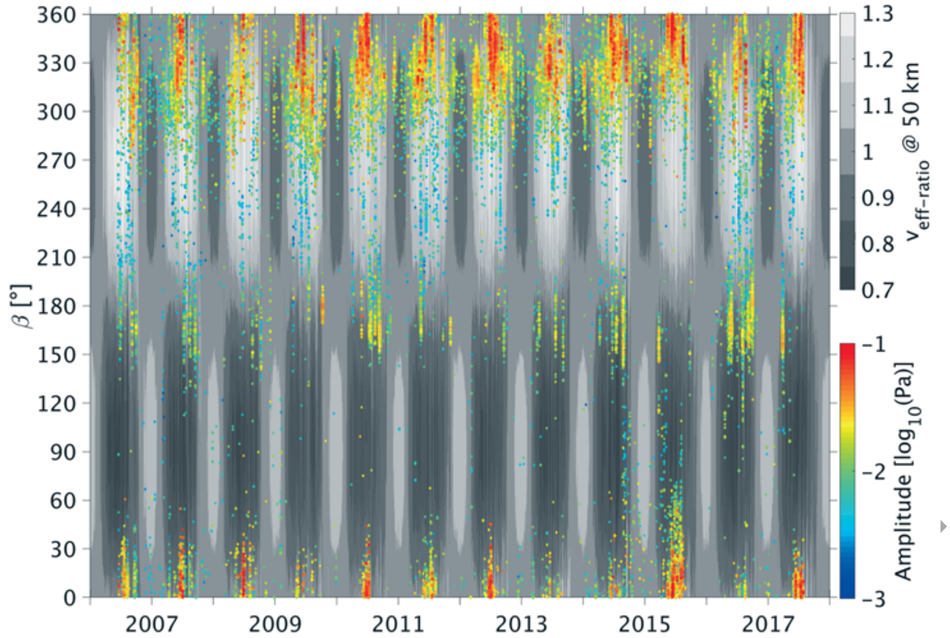

Figure 5: The temporal variation in back-azimuth (β) and amplitude (color-coded) of the MAW detections at IS02. Each dot represents a detection family. In the background, the ratio of v_{eff} at around 50 km and the surface is shown (gray scale), calculated from ECMWF data. This ratio indicates good propagation conditions from a direction towards the station when exceeding one – i.e., the presence of the ground-to-stratopause waveguide (light gray; dark gray: $v_{\text{eff-ratio}} < 1$). The detections from 150° to 210° originate from the Antarctic Peninsula. Detections from the north-northwest are associated with the Andes.

A special feature is the accumulation of cross-bearing results over the central USA. It is not directly associated with the Rocky Mountains. Although Bedard (1978) mentioned a MAW source region in the lee of the Rocky Mountains over Colorado, the seasonal appearance found here is in contradiction to his observations. It is detected at IS10 (β = 174°), IS53 (β = 96°), IS56 (β = 120°), and IS57 (β = 60°) only during summer (May to August). Therefore, the detections are more likely associated with the occurrence of severe storms in the central USA: During the 1960s and 1970s, severe storm cells that coincided with hail and tornadoes were observed causing the detection of infrasound signals with specific periods of 5 s to 62 s (Bowman and Bedard, 1971). Here, the detected properties and the season agree with those findings; hence, it is concluded that the IMS network also captures low-frequency infrasound from severe storms.

3.2 Propagation conditions

Propagation conditions are considered for validating detections from the identified source regions at selected stations. The focus is on the Southern Hemisphere hotspots since these can be associated with distinct mountainous ranges; whereas the most dominant hotspot in the Northern Hemisphere covers a large region with multiple mountain ranges.

Fig. 5 shows the time-series of PMCC detections at IS02 in the frequency range of MAWs (Table 1). Concerning the Andes, the majority of signals are detected during the winter when the atmospheric conditions are favorable for infrasound propagation from northwestern directions. During the summer, the number of detections is reduced by about 70 %. Accordingly, the detected amplitudes were largest in austral winter and smallest in summer, differing by half an order of magnitude.

The propagation between the southern Andes (49° S, 73° W) and IS02 (55° S, 68° W) was calculated using the 2D-FD ray-tracer (Section 2.4). As an example, Fig. 6 shows the modeling for July 2016. Accordingly, the propagation was modeled for each month between January 2007 and December 2016, based on the monthly-averaged along-path wind and temperature profiles.

The same simulations were done for IS08 (3,663 km to the north), IS09 (4,352 km to the north-northeast), IS14 (1,806 km to the northwest), IS21 (7,500 km to the east), and IS27 (4,043 km to the southeast). These stations also show detections most likely originating from the Andes hotspot. The ray-tracing results for the selected stations are summarized in Table 2. The statistics only account for parameters of stable eigen-ray solutions for stratospheric (I_s) and thermospheric (I_t) returns, if any. In addition, the accumulated atmospheric absorption along the propagation path (A_a, in dB) is provided.

During austral winter (May to August), ground-to-stratopause solutions resulted for IS02, IS08, and IS27. These agree with the PMCC detections and the cross-bearing results. In summer (November to February), simulations show that stratospheric ducting was rather unlikely for these stations. This fact also agrees with the PMCC detections. However, it is noted that IS21

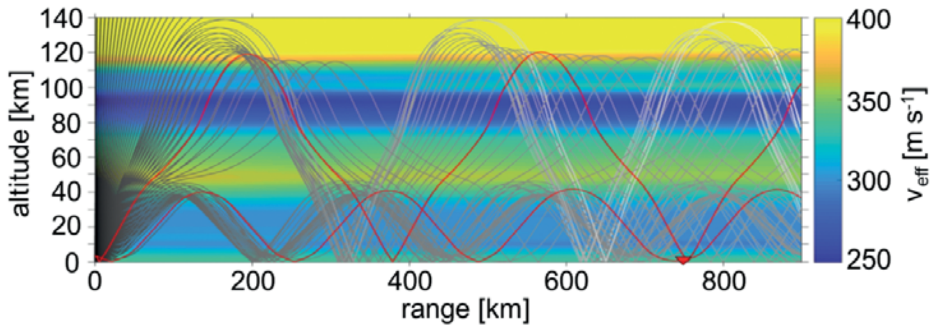

Figure 6: Ray-tracing paths between the southern Andes (0 km, 49° S, 73° W) and IS02 (red triangle) in southern Argentina are shown for July 2016. The source on the left was set to 3,200 m. The rays were started at angles of between 1° (upward) and 179° (downward). The modeled source frequency was 0.05 Hz, the upper center frequency threshold of MAWs; lower frequencies would be subject to even smaller atmospheric absorption rates. The stable eigen-ray solutions which best connect the source and receiver are depicted in red, for both the ground-to-stratopause and the ground-to-thermosphere waveguide.

Table 2: Ray-tracing results for selected stations detecting MAWs from the southern Andes. The numbers (0–10) reflect the number of simulation runs (one per year and month over 10 years) for which a stable eigen-ray solution was calculated between the source (49° S, 73° W) and the respective IMS station. Consequently, the numbers indicate the detection likelihood, about both stratospheric (I_s) and thermospheric (I_t) propagation paths. Besides, the mean and the standard deviation of atmospheric absorption (A_a) are given for these simulation runs. The source was set to an altitude of 3,200 m.

	IS02		IS08		IS21		IS27	
	I_s	I_t	I_s	I_t	I_s	I_t	I_s	I_t
Jan	0	10	0	10	10	8	0	9
Feb	0	10	3	10	6	8	0	8
Mar	3	10	6	9	4	9	6	9
Apr	8	10	6	10	0	10	9	7
May	9	10	8	9	0	10	9	9
Jun	10	9	5	9	0	10	9	5
Jul	10	10	7	6	0	10	9	4
Aug	9	10	5	6	0	10	9	6
Sep	7	10	9	9	0	10	9	7
Oct	2	10	9	7	5	6	5	9
Nov	0	10	7	8	10	8	1	9
Dec	0	10	4	10	10	7	0	9
$\overline{A_a}$ [dB]	0.1	3.8	0.7	15.0	1.3	19.4	0.4	17.3
σ_{A_a} [dB]	0.1	1.6	0.4	19.0	0.9	16.7	0.3	15.4

Table 3: Ray-tracing statistics as in Table 2, but for stations detecting a MAW source over New Zealand. Here, the source was set to an altitude of 3,000 m.

	IS05		IS07		IS22		IS36	
	I_s	I_t	I_s	I_t	I_s	I_t	I_s	I_t
Jan	10	7	10	8	8	9	0	10
Feb	10	10	10	7	6	10	0	10
Mar	0	10	0	10	0	10	3	10
Apr	0	10	0	10	0	10	10	6
May	0	10	0	10	0	10	10	6
Jun	0	10	0	10	0	10	10	4
Jul	0	10	0	9	0	9	10	4
Aug	0	10	0	10	0	10	8	4
Sep	3	9	0	10	2	9	5	10
Oct	9	8	4	10	3	10	0	10
Nov	10	9	3	9	9	10	0	10
Dec	9	10	10	9	10	9	0	10
$\overline{A_a}$ in dB	0.2	5.1	0.7	23.9	0.7	7.6	0.1	6.4
σ_{A_a} in dB	0.1	5.9	0.4	21.4	0.2	12.9	0.1	8.3

detected MAWs in April and July, although a westward propagation in the ground-to-stratopause waveguide was not modeled. Instead, ground-to-thermosphere ducting was successfully modeled for this station, despite a propagation range of 7,500 km. Moreover, the ground-to-thermosphere waveguide explained detections at IS13, IS14, IS21, and IS24 in the winter and at IS02 and IS09 in the summer. As a consequence, for explaining MAW detections upstream of the stratospheric jet, the low attenuation in the thermosphere is essential.

Similar results were obtained for MAW detections originating from the Southern Alps of New Zealand (44° S, 170° E). Increased detection numbers during winter (Section 3.1) agree with the ray-tracing results for IS36 (Table 3) because propagation within the ground-to-stratopause waveguide was only favored between April and September. A ray-tracing example for January and July 2016 is given in Figure S2 in the Supplements, showing a sharp effective sound speed gradient at the stratopause in July.

The seasonal variation in the number of detections at IS22 (Section 3.1) is contradictory to the stratospheric ray-tracing results, as these would suggest the maximum number during summer and the minimum during winter. Only the ground-to-thermosphere waveguide can explain the opposed cycle: According to the modeling, the thermospheric return heights were lowest in July (<110 km) and higher in January (>110 km), resulting in accumulated absorption rates of around 1 dB (July) and 9 dB (January), respectively, along the propagation paths. The low absorption rate in July can partly explain the large number of signal arrivals. Moreover, it is noted that single detections could result from small-scale fluctuations; for instance, upward-propagating GWs could temporarily establish a ground-to-stratosphere waveguide if such perturbations of the wind speed sufficiently increase the effective sound speed ratio in the upper stratosphere. Note that, for the troposphere, Damiens et al. (2018) also modeled an impact of OGWs and tropospheric winds on the acoustic wave field in mountainous regions. However, the high number of signals in winter would be more reasonable if the explanation can be found in the source generation mechanism.

3.3 Source conditions

The most dominant MAW source regions – the Southern Alps of New Zealand, the southern Andes, and the Tibetan Plateau – are characterized by strong tropospheric winds all around the year. Therefore, the monthly mean wind fields are not appropriate to analyze the source conditions during MAW events. Instead, the three-hourly dataset of the Modern-Era Retrospective analysis for Research and Applications, Version 2 (MERRA-2, Bosilovich et al., 2016) was used. The focus is on IS02 for the southern Andes and IS36 for New Zealand. These stations are nearest to the respective source regions, so propagation effects are minimized, and damping of the MAW amplitudes is smallest. The traveling times of the MAWs are shorter than the MERRA-2 time interval; for IS02, the average time is around 36 min (at distance $r = 749$ km and $v_{\mathrm{eff}} = 339\,\mathrm{m\,s^{-1}}$), and for IS36, this is around 51 min (at $r = 1{,}080$ km and $v_{\mathrm{eff}} = 350\,\mathrm{m\,s^{-1}}$), for stratospheric propagation (Hupe, 2018). The MAW detections were assigned the MERRA-2 wind speed and direction available before the signal was recorded. Five model levels were considered at those grid points best matching the hotspots' coordinates that were used in Section 3.2; these levels are 985 hPa (around 60 m above the ground – the model bottom level), 850 hPa (around 1.5 km), 700 hPa (around 3 km), 500 hPa (around 5.5 km), and 300 hPa (around 9.4 km). Unless otherwise stated, the following figures refer to the 700 hPa level.

The distributions in Fig. 7 show that the predominant wind speeds during MAW events originating from New Zealand (b), detected at IS36, are slightly higher than the climatological conditions (a). The maximum occurrence frequency of MAW detections from $\beta = 265°$ is at wind speeds of between $15\,\mathrm{m\,s^{-1}}$ and $35\,\mathrm{m\,s^{-1}}$ at 700 hPa (c), whereas the climatological wind distribution peaks below $15\,\mathrm{m\,s^{-1}}$. The maxima occur at cross-mountain wind directions of between 270° and 360° (b). At 500 hPa and 300 hPa, the comparisons show similar results, whereas, near the ground, the azimuth sector is narrower (315°±20°).

For IS02 and the southern Andes, the event-related occurrence frequency does not show a significant difference from the climatological wind conditions, and it also peaks between $15\,\mathrm{m\,s^{-1}}$ and $35\,\mathrm{m\,s^{-1}}$. Here, the distribution maxima appear to be a product of coincidence resulting from the climatological conditions; whereas, at IS36 and New Zealand, there is a tendency to increased wind speeds during MAW occurrence. The climatological difference might be an explanation for fewer detections from the Southern Alps at IS36 (around 10^4), compared to the southern Andes and IS02 (around 10^5).

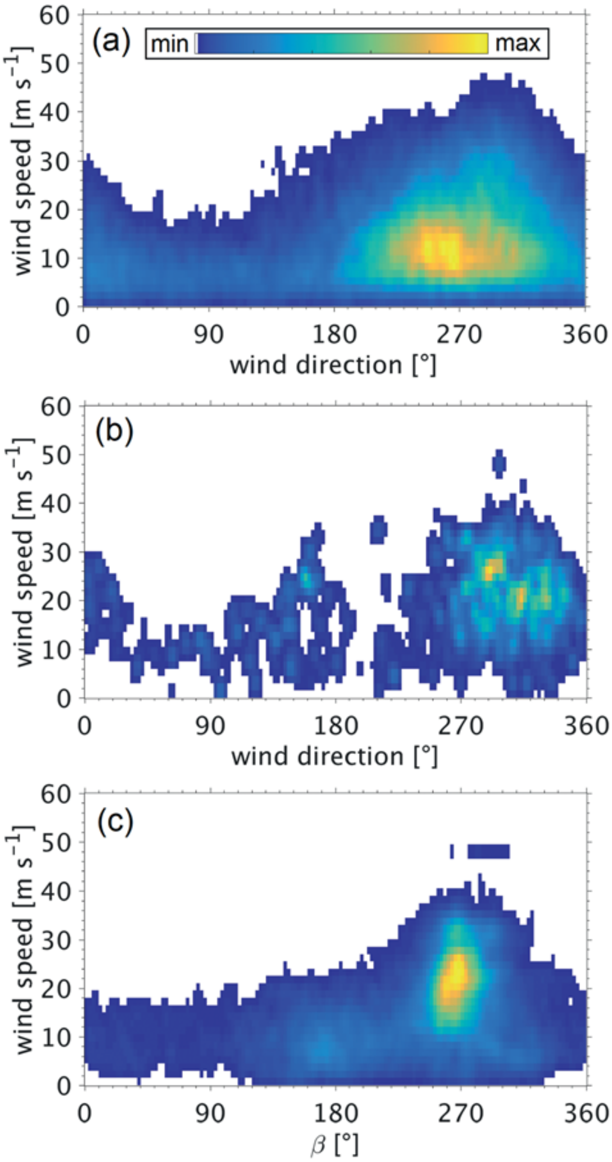

Figure 7: Evaluation of MERRA-2 tropospheric winds at 700 hPa over the Southern Alps of New Zealand (44° S, 170° E), and MAW detections at IS36. (a) Climatological distribution of the wind speed and direction, in the reference period 2003 to 2017; (b) distribution of the wind speed and direction during MAW detections that feature back-azimuths associated with the Southern Alps only; (c) wind speed over the Southern Alps during all MAW events detected at IS36 vs. the back-azimuths of these detections. The grid intervals are 2.5° (β and wind direction) and $1.5\,\mathrm{m\,s^{-1}}$ (wind speed). The distributions are normalized by the respective maximum values.

Fig. 8 shows a correlation between the detected MAW amplitudes at IS02 and the wind speeds over the source region. This correlation applies to altitudes up to around 5 km. Then the slopes representing the maxima

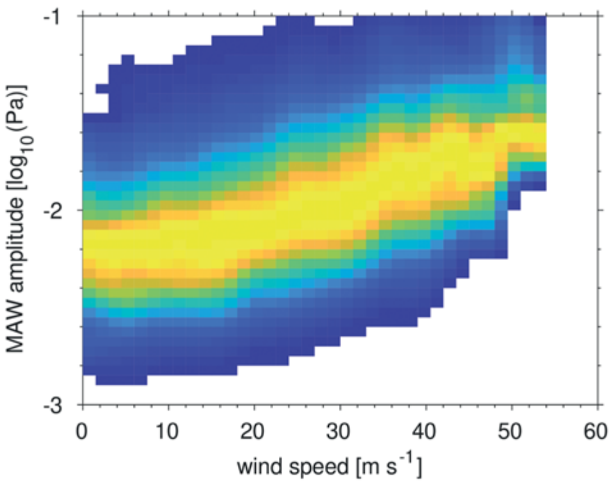

Figure 8: Correlation between detected MAW amplitudes and wind speeds at the source. This refers to wind speeds over the southern Andes at 700 hPa, and MAW detections at IS02 that are associated with the Andes ($\beta \geq 270°$ and $\beta \leq 45°$). The grid interval for the RMS amplitude is 0.05 $\log_{10}$(Pa) and the distribution is normalized per wind speed interval of 1.5 m s^{-1}; the color code is the same as in Fig. 7. The correlation for IS36 at the Southern Alps of New Zealand is comparable.

(yellow) incline with altitude (500 hPa and 300 hPa). As a conclusion, the correlation between the MAW amplitude and winds is strongest at layers near the orographic obstacle.

The mean wind conditions are relatively consistent throughout the year; at 700 hPa in the southern Andes, the annual mean wind speed is 19.5 m s^{-1} ($\sigma = \pm 9.2$ m s^{-1}), and the monthly means vary by ± 2 m s^{-1}. Consequently, if the wind is the primary quantity in the process of MAW generation, the preconditions for the excitation of MAWs do not significantly differ by season. Contrary to this is both the enhanced number of detections and the increased amplitudes in winter. According to Fig. 9, the MAW amplitudes originating from the southern Andes amount to 21 mPa in June ($\sigma = \pm 15$ mPa) and minimize in February (7 mPa, $\sigma = \pm 5$ mPa). Neither the mean nor the maximum climatological cross-mountain wind speeds exhibit a similar pattern.

The propagation conditions can explain the increased amplitudes at IS02 and IS36 during austral winter because the ground-to-stratopause waveguide is predominant (Section 3.2). This waveguide results in lower attenuation, compared to thermospheric propagation during summer, and enables larger amplitudes to be detected. It is worth adding that larger amplitudes generally allow better discrimination from noise in the infrasound recordings; hence, the enhanced number of PMCC detections could be related to the increased amplitudes. However, the results discussed for IS22 contradict that theory here, because the highest number of detections – even higher than at IS36, which is closer to the source region – was also found in winter despite the absence of a ground-to-stratopause waveguide. As a consequence, the source generation of MAWs must be subject to seasonal variability, and cross-mountain winds alone are not sufficient in this context. The positive correlation between cross-mountain winds and MAW amplitudes indicates that these winds contribute to the process of MAW excitation.

In terms of OGW occurrence, for which the discussed hotspots in the Southern Hemisphere are known (e.g., McLandress et al., 2000; Alexander and Teitelbaum, 2011; Hoffmann et al., 2016), static stability could be an additional quantity. Comparisons like in Figs. 7 and 8 do not indicate a correlation between the Brunt-Väisälä frequency, as a measure for stability, and the MAW occurrence although, in general, it seems that MAWs are detected during stable conditions. This fact can partly contribute to enhanced detection numbers during winter since the tropospheric conditions are generally more stable than during summer. Stable conditions in the atmospheric boundary layer reduce turbulent noise at the stations, which improves the detection capability (e.g., Pilger et al., 2015).

4 Comparison of the MAW hotspots with satellite-based GW hotspots

The question of whether a common source generation mechanism exists for MAWs and OGWs is assessed by comparing global GW hotspot maps with the identified source regions of MAWs. The global GW activity was obtained from the global GW climatology based on atmospheric infrared limb emissions observed by satellite (GRACILE), which was produced by Ern et al. (2017). GRACILE provides a climatology of GW parameters such as temperature variances, GW potential energy (GWPE), and absolute GW momentum flux (GWMF) in the middle atmosphere. Here, the GWMF data product from the Sounding of the Atmosphere using Broadband Emission Radiometry (SABER) instrument was used to estimate the global GW activity. SABER products are based on the period from February 2002 to January 2015 (13 years), and thus similar to the infrasound data set. The MAW source regions were compared with the GWMF at 30 km, the lowest available level. More precisely, the GWMF deviation from the zonal mean was calculated so that positive deviations indicate enhanced GW activity.

Lightning data were also taken into account to separate convectively-induced GWs from other sources like topography. Cecil (2015) produced the HRES monthly climatology of lightning activity. It provides mean flash rates per square kilometer and day in the middle of a month (Cecil et al., 2014) and was composed of data from the Optical Transient Detector and the Lightning Imaging Sensor.

In Fig. 10, color-coded lightning activity and GWMF are shown for January, April, July, and October. The black contour lines reflect the MAW source regions

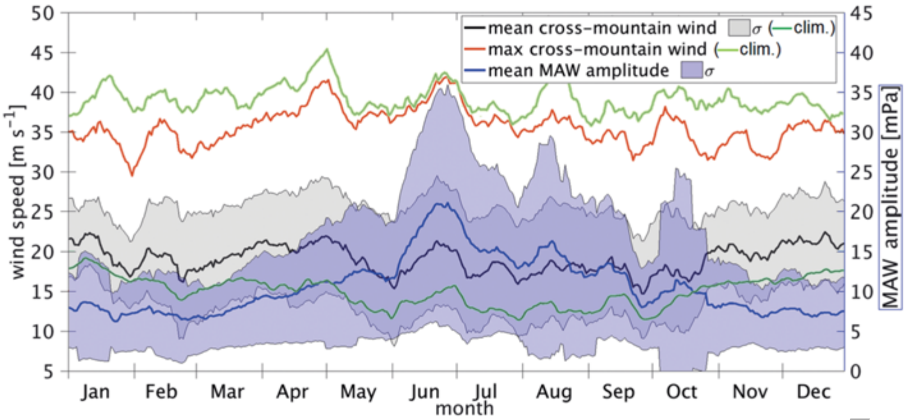

Figure 9: Annual amplitude variation of MAW detections from the southern Andes at IS02, and cross-mountain winds (directional wind components between 225° and 315°) at 700 hPa over the southern Andes. The event-based mean (black) and maximum (orange) MERRA-2 cross-mountain winds were calculated for each day of the year. The respective climatological daily mean and maximum values (2004 to 2017) are shown in green. A moving-average filter with a span of 15 d was applied to the data, and shaded areas depict the standard deviation (σ).

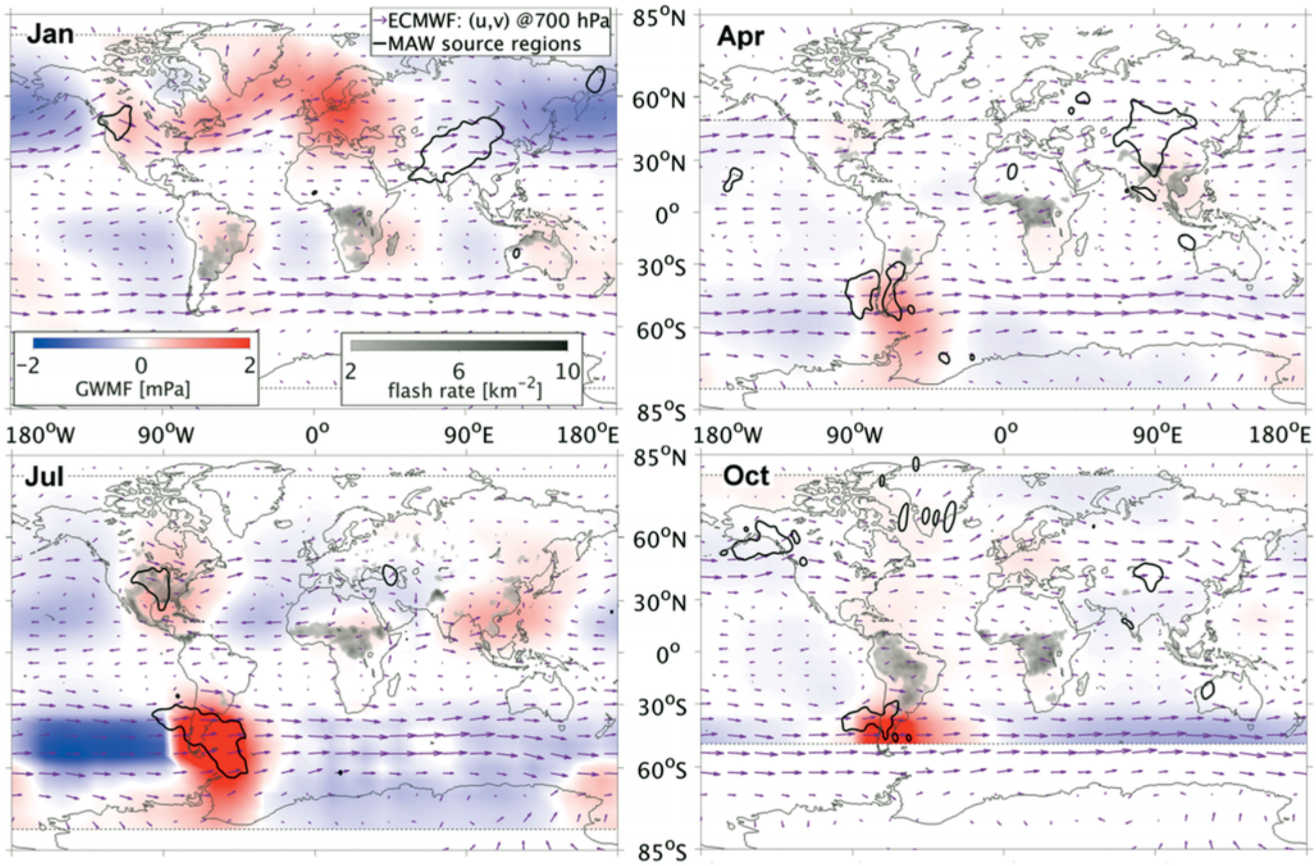

Figure 10: Comparison of GWMF (30 km) from GRACILE/SABER (Ern et al., 2017) with MAW hotspots as identified in Section 3. MAW contour lines equal the threshold of 0.05 normalized cross-bearing hits in Fig. 4. GWMF is given as the deviation from the zonal mean GWMF. Lightning activity (Cecil, 2015) is superimposed for areas with more than two flashes per km^{-2} (gray shades) to identify convectively induced GWs. With regard to Section 3.3, the ECMWF wind field (ECMWF, 2014) at 700 hPa (arrows) shows that mid-latitude GW hotspots and MAW hotspots coincide with high wind speeds. Note that dashed lines denote the latitudinal coverage of SABER in each month.

shown in Fig. 4. The 700 hPa level wind field of the ECMWF operational HRES analysis is added (monthly means for the period 2007 to 2016).

In the tropics and subtropics, the seasonal variation of enhanced GWMF agrees with increased lightning activity, so it is likely caused by deep convection within the Inter-tropical Convergence Zone. The allegedly found hotspot in the central USA between May and August is confirmed by these observations, in terms of severe storms.

In the southern Andes, the GWMF is strongly enhanced from April until October, which well agrees with the MAW hotspot. Also, weaker GWMF in March and November (not shown) coincides with the number of MAW detections. In the summer, the southern Andes exhibit no OGW hotspots, but rather GWs induced by deep convection (Hoffmann et al., 2013, figs. 6 to 10); obviously, this does not regularly cause infrasound signals like those detected in the central USA at a sufficient number of stations for the cross-bearing approach. This conclusion is supported by the fact that reports of severe storms including tornadoes in the very south of Argentina or Chile are not available.

As was discussed in Section 3, New Zealand's South Island is also a regular source region for MAWs although it does not appear in Fig. 10. Hoffmann et al. (2016), using satellite observations, identified New Zealand as one of the active source regions of OGWs in the Southern Hemisphere. They evaluated upstream and downstream variances in temperature perturbations at about 40 km altitude, based on 10 years of HRES satellite observations. GWMF is not enhanced over New Zealand in the GRACILE dataset. One reason is the coarse horizontal resolution of the GRACILE climatology – GW parameters were evaluated in bins of 30° × 20° (Ern et al., 2018). A second reason is the characteristic wind speed profile above mountain ranges at mid-latitudes. The atmospheric feature was pointed out by Kruse et al. (2016), termed the 'valve layer', which affects upward-propagating GWs. It is characterized by a wind speed minimum in the lower stratosphere (15–25 km) above a strong tropospheric jet-stream (Kruse et al., 2016). The wind speed minimum causes the vertical wavelength of an upward-propagating GW to shorten, which results in a steepening wave. If this causes the GW to break, momentum is deposited and will not reach the upper stratosphere, e.g., at 30 km. Large-amplitude GWs that are induced by strong tropospheric winds are particularly affected by the valve layer; whereas small-amplitude GWs are not forced to break and eventually propagate up to the mesosphere (e.g., Kaifler et al., 2015; Bramberger et al., 2017).

As an example, Fig. 11 shows monthly mean zonal wind speed profiles over the southern Andes (blue) and the Southern Alps of New Zealand (orange) in January (dashed line) and July (solid line). During summer (January), a critical level (Fritts and Alexander, 2003,) at around 22 km causes GW dissipation of upward-

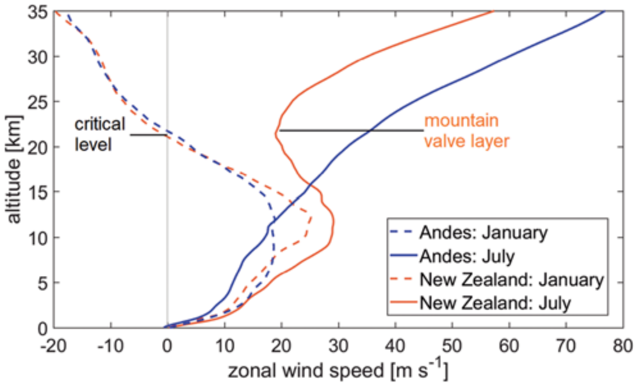

Figure 11: ECMWF HRES zonal wind speed profiles over the southern Andes (49° S, 73° W) and New Zealand's Southern Alps (44° S, 170° E) in January and July 2016. The winter profiles (July) differ because of the valve layer that is present over New Zealand, whereas the wind profile of the southern Andes would allow the upward propagation of OGWs into the upper stratosphere.

propagating OGWs in the lower stratosphere (e.g., Kaifler et al., 2015). In July, the zonal wind profiles differ such that there is a strong tropospheric jet at 10 km to 15 km over New Zealand ($\overline{u}$ = 28 m s^{-1}) and a relative wind minimum at 22 km ($\overline{u}$ = 18 m s^{-1}). This valve layer explains why the GW activity over New Zealand in winter remains unresolved at the lowest data level of the GRACILE climatology (30 km). It is noted that the feature of the valve layer disappears towards higher latitudes.

Enhanced GWMF does not match the MAW hotspot over the Tibetan Plateau in Fig. 10. Only in November and December (not shown), enhanced GWMF can be found in the north of the Tibetan Plateau. The tropospheric winds are relatively strong over the entire region all year round, similar to the southern Andes. Contrarily, the GWMF perturbations are strongest over Europe (Scandinavia), particularly in January. The weak GWMF over the Tibetan Plateau is also reasoned by the valve layer which regularly evolves above the tropospheric jet-stream during winter; for instance, the ECMWF HRES analysis yields a valve layer above the Pamir Mountains (38° N, 75° E), just west of the Tibetan Plateau. In 2016, for example, a mean zonal wind maximum of 32 m s^{-1} was at 10 km and a local minimum of 14 m s^{-1} at 19 km in January (Figure S3 in the Supplements). The critical level was at 15 km in July 2016.

Zeng et al. (2017) reported evidence of OGWs above the Tibetan Plateau. They evaluated nine years of satellite data from the lower stratosphere (15–30 km) and found OGWs during winter and spring. Moreover, Alexander et al. (2008) found that enhanced GWPE up to the tropopause was generally filtered at levels of low wind speed below 30 km altitude.

The MAW hotspot of the coastal mountain ranges in North America agrees with enhanced GWMF in January. In November, the GWMF deviation is also positive in this region; whereas it equals the zonal mean in

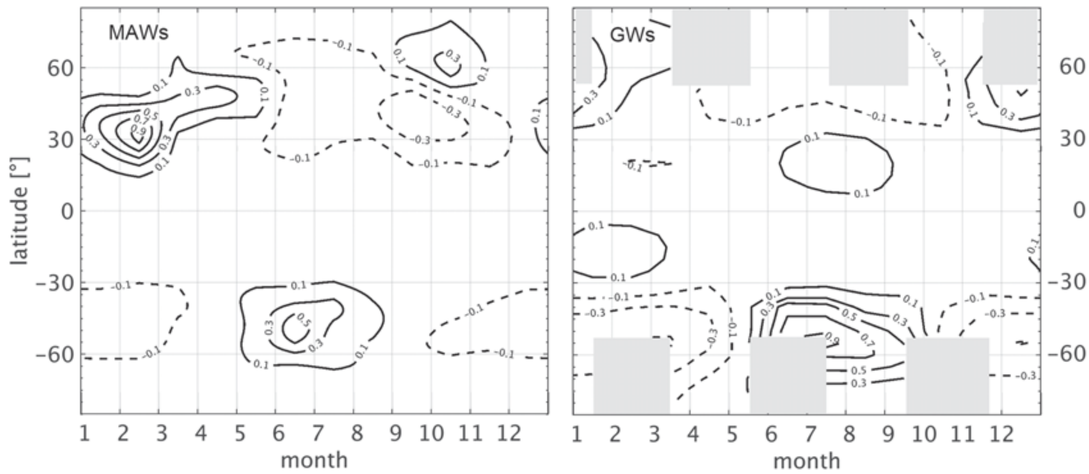

Figure 12: Comparison of the annual variability of zonal mean MAW hotspots and zonal mean stratospheric GWMF. Variability is reflected as the deviation from the zonal mean, normalized by its absolute maximum. Left: MAW source regions, as deduced from the cross-bearing hits shown in Fig. 4. Right: Stratospheric GWMF at 30 km altitude, as deduced from GRACILE's global map data.

October. Hoffmann et al. (2017) argued that low stratospheric wind speeds, preventing GWs from propagating upward in this region, result in only a few stratospheric GW observations. They also identified the East Siberian Mountains as a source region of OGWs. Here, ECMWF data show critical levels in both January and July 2016 (not shown).

At high latitudes in general, the distribution of IMS infrasound arrays compared to the source regions is relatively coarse which prevents for obtaining enough cross-bearing results for events like MAWs. It is worth mentioning that the station distribution meets the detection capability required for the monitoring of the CTBT (Le Pichon et al., 2019). Nevertheless, the Antarctic Peninsula and the Trans-antarctic Mountains in the Southern Hemisphere, which are strong OGW hotspots (Hoffmann et al., 2013; Hoffmann et al., 2016; Jewtoukoff et al., 2015), are detected at IMS stations – the Antarctic Peninsula at IS02 (β = 170°) and IS27 (β = 250°) during spring and autumn, and the Trans-antarctic Mountains at IS05 (β = 200°) and IS36 (β = 180°) during winter.

In the Northern Hemisphere, wide regions of positive GWMF perturbations are detached from lightning and MAW activity at middle and high latitudes during winter. Indeed, GW hotspots have been observed in Scandinavia (e.g., Rapp et al., 2018), Greenland (Leutbecher and Volkert, 2000; Limpasuvan et al., 2007), and the UK (Hoffmann et al., 2013; Hoffmann et al., 2017). Although pairs of IMS infrasound stations detect MAWs potentially originating from those regions, the multitude of possible sources and the dominance of detections from the Tibetan Plateau complicate the determination of further MAW hotspots in the Northern Hemisphere. The fact that many IMS infrasound stations surround the Tibetan Plateau region may cause an overestimation of this hotspot. Nevertheless, the station markers in Fig. 4 indicate high detection numbers which still imply this hotspot to be very active.

Fig. 12 summarizes the global MAW and GW activity. The MAW activity was calculated as the number of cross-bearing hits per 3° × 3°. The contours denote the deviation from the zonal mean, normalized by the overall maximum. Positive (negative) values indicate enhanced (reduced) MAW activity relative to the annual zonal mean; hence, the global maximum is one. Analogously, the zonal mean GW activity was calculated, based on the GWMF of GRACILE at 30 km.

The qualitative agreement between MAW and GW activity is good. The differences in the Northern Hemisphere, and at high latitudes in general, are caused by the distribution of infrasound stations relative to potential MAW and OGW source regions. Significant tropical sources of MAWs are missing due to the lack of strong winds. At mid-latitudes, especially in the Southern Hemisphere, the patterns of MAW and GW activity are very similar. Quantitatively, the difference between GW and MAW activity traces back to the location of the respective global maxima. The strongest GW activity is located in the southern Andes region; whereas the strongest MAW activity is excited over central Asia (Tibetan Plateau and surrounding mountain ranges) and not reflected by GRACILE for the reasons mentioned above. This difference, however, poses the question if the source generation of MAWs is primarily related to the tropospheric cross-mountain winds – these are stronger over the Tibetan Plateau (Figure S3 in the Supplements) than over the Andes (Fig. 11). The MAW generation could also be linked to the excitation, or breaking, of OGWs.

5 Further discussion of the results

The results of Sections 3 and 4 imply that the tropospheric winds play a significant role in the source generation of MAWs. Not only the wind direction (roughly perpendicular to mountain ranges) but also the wind speed at altitudes up to around 5 km correlates with

MAW occurrence and amplitude. The variation in amplitude is ascribed to the different propagation waveguides in the atmosphere since the absorption of an acoustic signal is lower in the surface-to-stratopause waveguide. For the variation in the number of detections, however, the cross-mountain winds in the Southern Hemisphere hotspots do not provide a sufficient explanation since these are consistent throughout a year. The same result can be anticipated for the Tibetan Plateau, given the enhanced number of detections during winter as opposed to strong tropospheric winds during both summer and winter. So which process or quantity, in addition to the tropospheric winds, is essential for the generation and observation of MAWs?

Stable stratification was considered to be another meteorological precondition for MAW generation, and this would be shared with OGWs. Also, a layer of increased stability near the mountain top favors larger amplitude OGWs. Although it is reasonable that MAW detections are favored during stable conditions, which result in less noise (due to limited turbulence) at the stations in winter, a clear correlation between enhanced stability and MAW occurrence, or amplitude, was not found. A possible reason is that, in terms of the detection capability, strong tropospheric winds counteract the effect of stable conditions at a station. Strong winds produce not only large MAW amplitudes at the source but also high noise levels at the receiver. Stable conditions cause lower noise levels, enabling the detection of smaller amplitudes.

OGWs can also be induced by nonstationary winds flowing over mountainous regions, resulting in horizontally propagating GWs. In this case of non-zero phase speed GWs, the valve layer and especially the critical level considered above are not relevant. Shevov et al. (2000) found that OGWs excited by nonstationary winds propagate into the mesosphere where they cause temperature perturbations when dissipating. Following Chunchuzov (1994), nonstationary winds are also a cause of acoustic wave excitation. Such infrasound signals would comprise of acoustic impulses that result from a superposition of strong wind gusts in nonstationary flows around mountains. Analyzing this in the future requires the use of local wind and turbulence measurements.

The results of the comparison in Section 4 show, in general, a clear agreement between the MAW and GW source regions. When considering the effect of the valve layer, which limits the upward propagation of GWs, the good agreement at the majority of MAW hotspots allows for the hypothesis that OGWs are included in the process of MAW generation. If not being an indirect link which could arise from the topographic and meteorological preconditions, GW breaking at different altitudes could be such a mechanism. Alternatively, the MAW source generation mechanism could be related to the tropospheric occurrence of OGWs, independent of their upward propagation into the middle atmosphere. This also includes propagating OGWs below the tropopause level caused by nonstationary winds.

Nonstationary tropospheric winds can comprise of a wide spectrum of spatial and temporal fluctuations. This implies that these winds potentially excite different wave scales, covering both MAW and OGW frequencies. Chunchuzov (1994) stated that breaking stationary OGWs can contribute to nonstationary flows due to turbulence production. Therefore, this theory would justify a common source of MAWs and (nonstationary) OGWs, but also a direct link between (stationary) OGWs and the MAW excitation.

In the latter case, it is presumed that OGWs induce MAWs. The principle behind this theory is that breaking OGWs decay into higher frequency waves and produce turbulent flows. Infrasonic waves would either be a direct product of this process chain, which is in line with the energy cascade, or a secondary product according to the theory of nonstationary flows. A strong indication for the direct infrasound production from breaking GWs has been provided by Lund et al. (2018). They modeled the GW field above the Andes. As a result of thermodynamic instabilities in the mesosphere causing the GWs to break, these produced upstream- and downstream-propagating acoustic waves. Previously, Thomas et al. (1974) had rejected the theory of breaking lee waves being involved in the MAW production, which relied upon the evaluation of power spectra slopes of selected MAW events. Following the findings of Lund et al. (2018), the valve layers over New Zealand or the Tibetan Plateau could also be altitude layers where MAWs are excited as a result of breaking stationary OGWs. The correlation between MAW amplitude and wind speeds is reasonable in this context.

However, for clarifying the exact source generation mechanism based on the two theories discussed above, more detailed analyses of MAW events will be necessary. Instead of analyzing the monthly MAW detections stacked over 15 years, shorter and subsequent time windows or even an event-based evaluation will allow further conclusions on the source generation mechanism. GW models need to be incorporated in such a study.

Concerning feedback mechanisms within turbulent flows, the impact of OGWs on the acoustic wave field is of great interest. Damiens et al. (2018) have addressed this topic by modeling the effect of tropospheric winds, OGWs, and low-altitude critical levels on the sound propagation in mountainous regions. Sabatini et al. (2019) have recently investigated the infrasound propagation through turbulent layers caused by breaking OGWs.

Our study focused on the determination and characterization of global MAW hotspots compared to GW hotspots derived from satellite data and showed the potential of the IMS infrasound network for assessing such a rarely studied type of atmospheric wave. At high latitudes, however, the station distribution relative to mountain ranges complicated the robust identification of MAW source regions using the elaborated cross-bearing method. A future study could enhance this method incorporating weighting functions for the different stations. These should reflect station and detection parameters, such as the number of sensors and family sizes (Landès et al., 2012), respectively. Considering additional infrasound stations in Europe (Pilger et al., 2018) and the USA (Hedlin, 2015) will allow for better discriminating source regions at high latitudes in the Northern Hemisphere.

6 Summary and conclusions

In this paper, a rarely investigated infrasound phenomenon – the MAW – was studied, and global source regions were identified using infrasound measurements of the IMS network. The dataset that covers more than 15 years was processed with the PMCC algorithm, and a cross-bearing method was applied to the monthly-averaged low-frequency detections between 0.02 Hz to 0.05 Hz. A comprehensive analysis of the global hotspots towards both meteorological source and propagation conditions was carried out.

The newly identified hotspot in central Asia appears to be the strongest one worldwide. In addition, the southern Andes and the Southern Alps of New Zealand are noticeable source regions of MAW since these are also OGW hotspots in the Southern Hemisphere. At high latitudes, the station distribution is relatively coarse, compared to lower latitudes. This has limited the results of the elaborated cross-bearing method in these latitudes. However, with IS03, an additional station recently started its operation in Antarctica, and yet another station is planned on the Antarctic Peninsula (IS54). These may further improve the results of the cross-bearing.

Detections originating from MAWs were generally observed all year round. The ground-to-stratosphere waveguide enables larger amplitudes to be detected at the receivers than the ground-to-thermosphere waveguide. However, in contrast to phenomena of higher frequencies than MAWs, the ground-to-thermosphere waveguide proved to be essential to explain occasions of MAW detections at even long distances of several thousand kilometers. The weak absorption at these low frequencies still favors small-amplitude detections at such distances.

The event-based wind analysis revealed a positive correlation between the MAW amplitude and the cross-mountain wind speed over the southern Andes and New Zealand. Conclusively, a MAW hotspot where the cross-mountain wind speed varies with the season will exhibit an annual variation in recorded MAW amplitudes. In the Southern Hemisphere source regions analyzed here, the wind conditions are consistent throughout a year. The seasonal variation in MAW amplitudes was therefore primarily associated with the present waveguides. Concerning the seasonal variation in the number of detections, however, an additional physical process was required in the source generation mechanism to explain the peak in winter. Static stability was discussed in this context, but it affects the stations' detection capability rather than the excitation of MAWs, to first order.

A comparison with GW parameters from stratospheric satellite data showed that the dominant MAW hotspots convincingly matched those of well-accepted source regions of OGWs. The characteristic valve layer in the lower stratosphere can explain exceptions found in the comparison. Breaking GWs at different altitudes are a possible source of infrasound waves originating from mountainous regions. This link with GWs recalls the static stability to be indirectly involved since stable stratification is a precondition for OGWs. Since further theories, such as the vortex shedding of turbulent flows at mountains, cannot be excluded in general, the exact excitation mechanism should be further addressed in a future study. This should incorporate GW models and analyze MAWs within smaller time windows for elaborating if breaking OGWs directly excite MAWs or if nonstationary winds even simultaneously release acoustic and GWs at mountains. If it turns out that OGWs induce the MAWs, the IMS infrasound network will be a unique ground-based system able to monitor the OGW activity continuously and globally.

Acknowledgments

The authors thank the editor Alexander Gohm and the two anonymous reviewers who provided useful comments for improving this manuscript. The research leading to these results has been performed within ARISE2 (http://ARISE-project.eu) that received funding from the European Commission's Horizon 2020 program under grant agreement 653980. The operational ECMWF HRES atmospheric model analysis defined by the IFS is available at https://www.ecmwf.int/en/forecasts/datasets (last access: 28 February 2019). MERRA-2 data can be accessed through the NASA Goddard Earth Sciences Data Information Services Center via https://gmao.gsfc.nasa.gov/reanalysis/MERRA-2/data_access (last access: 06 May 2019). The International Data Centre in Vienna is acknowledged for providing the IMS infrasound data. The views of the authors do not necessarily reflect the views of the CTBT Organization Preparatory Commission.

Abbreviations

β	back-azimuth (direction of origin)
A_a	Atmospheric Absorption
I_s	Signal return from stratospheric ducting
I_t	Signal return from thermospheric ducting
2D	two-dimensional
2D-FD	two-dimensional finite differences (ray-tracing model)
CTBT	Comprehensive Nuclear-Test-Ban Treaty
ECMWF	European Center for Medium-Range Weather Forecasts

GRACILE	Global Gravity Wave Climatology Based on Atmospheric Infrared Limb Emissions Observed by Satellite
(O)GW	(Orographic) Gravity Wave
GWMF	Gravity Wave Momentum Flux
GWPE	Gravity Wave Potential Energy
HRES	High-Resolution
IFS	Integrated Forecast System
IMS	International Monitoring System
ISxx	Infrasound Station (+number); e.g., IS02 is IMS infrasound station no. 2
MAW	Mountain-Associated Wave
MERRA-2	Modern-Era Retrospective Analysis for Research and Applications, Version 2
PMCC	Progressive Multi-Channel Correlation
SABER	Sounding of the Atmosphere Using Broadband Emission Radiometry

References

Alexander, M.J., H. Teitelbaum, 2011: Three-dimensional properties of Andes mountain waves observed by satellite: A case study. – J. Geophys. Res. **116**, D23110, DOI: 10.1029/2011JD016151.

Alexander, S.P., T. Tsuda, Y. Kawatani, 2008: COSMIC GPS Observations of Northern Hemisphere winter stratospheric gravity waves and comparisons with an atmospheric general circulation model. – Geophys. Res. Lett. **35**, L10808, DOI: 10.1029/2008GL033174.

Alexander, P., D. Luna, P. Llamedo, A. de la Torre, 2010: A gravity waves study close to the Andes mountains in Patagonia and Antarctica with GPS radio occultation observations. – Ann. Geophys. **28**, 587–595, DOI: 10.5194/angeo-28-587-2010.

Assink, J.D., A. Le Pichon, E. Blanc, M. Kallel, L. Khemiri, 2014: Evaluation of wind and temperature profiles from ECMWF analysis on two hemispheres using volcanic infrasound. – J. Geophys. Res. **119**, 8659–8683, DOI: 10.1002/2014JD021632.

Bedard, A.J., 1978: Infrasound Originating Near Mountainous Regions in Colorado. – J. Appl. Meteor. **17**, 1014–1022, DOI: 10.1175/1520-0450(1978)017<1014:IONMRI>2.0.CO;2.

Blanc, E., L. Ceranna, A. Hauchecorne, A. Charlton-Perez, E. Marchetti, L.G. Evers, T. Kvaerna, J. Lastovicka, L. Eliasson, N.B. Crosby, P. Blanc-Benon, A. Le Pichon, N. Brachet, C. Pilger, P. Keckhut, J.D. Assink, P.S.M. Smets, C.F. Lee, J. Kero, T. Sindelarova, N. Kämpfer, R. Rüfenacht, T. Farges, C. Millet, S.P. Näsholm, S.J. Gibbons, P.J. Espy, R.E. Hibbins, P. Heinrich, M. Ripepe, S. Khaykin, N. Mze, J. Chum, 2018: Toward an Improved Representation of Middle Atmospheric Dynamics Thanks to the ARISE Project. – Surv. Geophys. **39**, 171–225, DOI: 10.1007/s10712-017-9444-0.

Bosilovich, M.G., R. Lucchesi, M. Suarez, 2016: MERRA-2: File Specification. – Office Note No. 9 (V1.1), Global Modeling and Assimilation Office, Greenbelt, MD, USA, last accessed: 18 August 2018. 73 pp.

Bowman, H.S., A.J. Bedard, 1971: Observations of Infrasound and Subsonic Disturbances Related to Severe Weather. – Geophys. J.R. Astron. Soc. **26**, 215–242, DOI: 10.1111/j.1365-246x.1971.tb03396.x.

Bramberger, M., A. Dörnbrack, K. Bossert, B. Ehard, D.C. Fritts, B. Kaifler, C. Mallaun, A. Orr, P.D. Pautet, M. Rapp, M.J. Taylor, S. Vosper, B.P. Williams, B. Witschas, 2017: Does Strong Tropospheric Forcing Cause Large-Amplitude Mesospheric Gravity Waves? A DEEPWAVE Case Study. – J. Geophys. Res. **122**, 11422–11443, DOI: 10.1002/2017JD027371.

Campbell, W.H., J.M. Young, 1963: Auroral zone observations of infrasonic pressure waves related to ionospheric disturbances and geomagnetic activity. – J. Geophys. Res. **68**, 5909–5916.

Cansi, Y., 1995: An automatic seismic event processing for detection and location: The P.M.C.C. Method. – Geophys. Res. Lett. **22**, 1021–1024, DOI: 10.1029/95GL00468.

Cecil, D.J., 2015: LIS/OTD Gridded Lightning Climatology Data Collection, Version 2.3.2015 [0.5 Degree High Resolution Monthly Climatology (HRMC)]. – Data set, NASA EOSDIS Global Hydrology Resource Center Distributed Active Archive Center, Huntsville, AL, USA, DOI: 10.5067/LIS/LIS-OTD/DATA311. (accessed: 13 August 2018).

Cecil, D.J., D.E. Buechler, R.J. Blakeslee, 2014: Gridded lightning climatology from TRMM-LIS and OTD: Dataset description. – Atmos. Res. **135–136**, 404–414, DOI: 10.1016/j.atmosres.2012.06.028.

Ceranna, L., R.S. Matoza, P. Hupe, A. Le Pichon, M. Landès, 2019: Systematic Array Processing of a Decade of Global IMS Infrasound Data. – In: A. Le Pichon, E. Blanc, A. Hauchecorne (Eds.): Infrasound Monitoring for Atmospheric Studies – Challenges in Middle-atmosphere Dynamics and Societal Benefits, 471–482. Springer, Dordrecht, the Netherlands, DOI: 10.1007/978-3-319-75140-5_13.

Chanaud, R.C., 1970: Aerodynamic Whistles. – Sci. Amer. **222**, 40–47, DOI: 10.1038/scientificamerican0170-40.

Chimonas, G., 1977: A Possible Source Mechanism for Mountain-Associated Infrasound. – J. Atmos. Sci. **34**, 806–811, DOI: 10.1175/1520-0469(1977)034<0806:APSMFM>2.0.CO;2.

Christie, D.R., P. Campus, 2010: The IMS Infrasound Network: Design and Establishment of Infrasound Stations. – In: A. Le Pichon, E. Blanc, and A. Hauchecorne (Eds.): Infrasound Monitoring for Atmospheric Studies, 29–75. Springer, Dordrecht, the Netherlands, DOI: 10.1007/978-1-4020-9508-5_2.

Chunchuzov, I.P., 1994: On a Possible Generation Mechanism for Nonstationary Mountain Waves in the Atmosphere. – J. Atmos. Sci. **51**, 2196–2206, DOI: 10.1175/1520-0469(1994)051<2196:OAPGMF>2.0.CO;2.

Cook, R.K., 1969: Atmospheric sound propagation. – In: D. Atlas and others (Eds.): NAS-NRC Atmospheric Exploration by Remote Probes, volume 2, National Academy of Sciences – National Research Council, Panel on Remote Atmospheric Probing, Rockville, MD, USA, 633–669.

CTBT Organization, 2019: 1996: CTBT: A Long-Sought Success. – https://www.ctbto.org/the-treaty/, last accessed: 23 April 2019.

Damiens, F., C. Millet, F. Lott, 2018: An investigation of infrasound propagation over mountain ranges. – J. Acoust. Soc. Amer. **143**, 563–574, DOI: 10.1121/1.5020783.

De Groot-Hedlin, C.D., M.A.H. Hedlin, 2015: A method for detecting and locating geophysical events using groups of arrays. – Geophys. J. Int. **203**, 960–971, DOI: 10.1093/gji/ggv345.

De Groot-Hedlin, C.D., M.A.H. Hedlin, D.P. Drob, 2010: Atmospheric Variability and Infrasound Monitoring. – In: A. Le Pichon, E. Blanc, A. Hauchecorne (Eds.): Infrasound Monitoring for Atmospheric Studies, 475–507. Springer, Dordrecht, the Netherlands, DOI: 10.1007/978-1-4020-9508-5_15.

Donn, W.L., D. Rind, 1972: Microbaroms and the Temperature and Wind of the Upper Atmosphere. – J. Atmos. Sci. **29**, 156–172, DOI: 10.1175/1520-0469(1972)029<0156:MATTAW>2.0.CO;2.

Dörnbrack, A., T. Gerz, U. Schumann, 1995: Turbulent breaking of overturning gravity waves below a critical level. – Appl. Sci. Res. **54**, 163–176, DOI: 10.1007/bf00849114.

Drob, D.P., J.M. Picone, M. Garcés, 2003: Global morphology of infrasound propagation. – J. Geophys. Res. **108**, 4680, DOI: 10.1029/2002JD003307.

Drob, D.P., J.T. Emmert, G. Crowley, J.M. Picone, G.G. Shepherd, W. Skinner, P. Hays, R.J. Niciejewski, M. Larsen, C.Y. She, J.W. Meriwether, G. Hernandez, M.J. Jarvis, D.P. Sipler, C.A. Tepley, M.S. O'Brien, J.R. Bowman, Q. Wu, Y. Murayama, S. Kawamura, I.M. Reid, R.A. Vincent, 2008: An empirical model of the Earth's horizontal wind fields: HWM07. – J. Geophys. Res. **113**, A12304, DOI: 10.1029/2008ja013668.

ECMWF, 2014: Part III: Dynamics and Numerical Procedures. IFS DOCUMENTATION – Cy40r1, ECMWF, Reading, United Kingdom last accessed: 10 September 2018.

Ehard, B., P. Achtert, A. Dörnbrack, S. Gisinger, J. Gumbel, M. Khaplanov, M. Rapp, J. Wagner, 2016: Combination of Lidar and Model Data for Studying Deep Gravity Wave Propagation. – Mon. Wea. Rev. **144**, 77–98, DOI: 10.1175/MWR-D-14-00405.1.

Ehard, B., B. Kaifler, A. Dörnbrack, P. Preusse, S.D. Eckermann, M. Bramberger, S. Gisinger, N. Kaifler, B. Liley, J. Wagner, M. Rapp, 2017: Horizontal propagation of large-amplitude mountain waves into the polar night jet. – J. Geophys. Res. **122**, 1423–1436, DOI: 10.1002/2016JD025621.

Ern, M., Q.T. Trinh, P. Preusse, J.C. Gille, M.G. Mlynczak, J.M. Russell, M. Riese, 2017: GRACILE: A comprehensive climatology of atmospheric gravity wave parameters based on satellite limb soundings. *PANGAEA*, link to data in netcdf format, DOI: 10.1594/PANGAEA.879658. (supplement to Ern et al. (2018), accessed: 27 July 2018).

Ern, M., Q.T. Trinh, P. Preusse, J.C. Gille, M.G. Mlynczak, J.M. Russell III, M. Riese, 2018: GRACILE: a comprehensive climatology of atmospheric gravity wave parameters based on satellite limb soundings. – Earth Syst. Sci. Data **10**, 857–892, DOI: 10.5194/essd-10-857-2018.

Evers, L.G., 2008: The inaudible symphony: on the detection and source identification of atmospheric infrasound. – Ph.D. thesis, Delft University of Technology, Delft, the Netherlands. 160 pp.

Evers, L.G., H.W. Haak, 2010: The Characteristics of Infrasound, its Propagation and Some Early History. – In: A. Le Pichon, E. Blanc, A. Hauchecorne (Eds.): Infrasound Monitoring for Atmospheric Studies, 3–27. Springer, Dordrecht, the Netherlands, DOI: 10.1007/978-1-4020-9508-5_1.

Fritts, D.C., M.J. Alexander, 2003: Gravity wave dynamics and effects in the middle atmosphere. – Rev. Geophys. **41**, 1003, DOI: 10.1029/2001RG000106.

Gill, A.E., 1982: Volume 30 of International Geophysics. – Academic Press, San Diego, CA, USA.

Greene, G.E., J. Howard, 1975: Natural Infrasound: A One Year Global Study. – Tech. Report 317-WPL-37, NOAA, Boulder, CO, USA.

Hoffmann, L., X. Xue, M.J. Alexander, 2013: A global view of stratospheric gravity wave hotspots located with Atmospheric Infrared Sounder observations. – J. Geophys. Res. **118**, 416–434, DOI: 10.1029/2012JD018658.

Hoffmann, L., A.W. Grimsdell, M.J. Alexander, 2016: Stratospheric gravity waves at Southern Hemisphere orographic hotspots: 2003–2014 AIRS/Aqua observations. – Atmos. Chem. Phys. **16**, 9381–9397, DOI: 10.5194/acp-16-9381-2016.

Hoffmann, L., R. Spang, A. Orr, M.J. Alexander, L.A. Holt, O. Stein, 2017: A decadal satellite record of gravity wave activity in the lower stratosphere to study polar stratospheric cloud formation. – Atmos. Chem. Phys. **17**, 2901–2920, DOI: 10.5194/acp-17-2901-2017.

Holton, J.R., 1983: The Influence of Gravity Wave Breaking on the General Circulation of the Middle Atmosphere. – J. Atmos. Sci. **40**, 2497–2507, DOI: 10.1175/1520-0469(1983)040<2497:TIOGWB>2.0.CO;2.

Hupe, P., 2018: Global infrasound observations and their relation to atmospheric tides and mountain waves. Ph.D. thesis, Ludwig-Maximilians-Universität München, Germany. – https://edoc.ub.uni-muenchen.de/23790/, last accessed: 14 May 2019. 189 pp.

Hupe, P., L. Ceranna, C. Pilger, M. De Carlo, A. Le Pichon, B. Kaifler, M. Rapp, 2019: Assessing middle atmosphere weather models using infrasound detections from microbaroms. – Geophys. J. Int. **216**, 1761–1767, DOI: 10.1093/gji/ggy520.

Jewtoukoff, V., A. Hertzog, R. Plougonven, de la A. Cámara, F. Lott, 2015: Comparison of Gravity Waves in the Southern Hemisphere Derived from Balloon Observations and the ECMWF Analyses. – J. Atmos. Sci. **72**, 3449–3468, DOI: 10.1175/JAS-D-14-0324.1.

Jiang, Q., J.D. Doyle, S.D. Eckermann, B.P. Williams, 2019: Stratospheric Trailing Gravity Waves from New Zealand. – J. Atmos. Sci. **76**, 1565–1586, DOI: 10.1175/JAS-D-18-0290.1.

Kaifler, B., N. Kaifler, B. Ehard, A. Dörnbrack, M. Rapp, D.C. Fritts, 2015: Influences of source conditions on mountain wave penetration into the stratosphere and mesosphere. – Geophys. Res. Lett. **42**, 9488–9494, DOI: 10.1002/2015GL066465.

Koch, K., C. Pilger, 2018: Infrasound observations from the site of past underground nuclear explosions in North Korea. – Geophys. J. Int. **216**, 182–200, DOI: 10.1093/gji/ggy381.

Kruse, C.G., R.B. Smith, S.D. Eckermann, 2016: The Midlatitude Lower-Stratospheric Mountain Wave 'Valve Layer". – J. Atmos. Sci. **73**, 5081–5100, DOI: 10.1175/jas-d-16-0173.1.

Landès, M., L. Ceranna, A. Le Pichon, R.S. Matoza, 2012: Localization of microbarom sources using the IMS infrasound network. – J. Geophys. Res. **117**, D06102, DOI: 10.1029/2011JD016684.

Landès, M., A. Le Pichon, N.M. Shapiro, G. Hillers, M. Campillo, 2014: Explaining global patterns of microbarom observations with wave action models. – Geophys. J. Int. **199**, 1328–1337, DOI: 10.1093/gji/ggu324.

Larson, R.J., L.B. Craine, J.E. Thomas, C.R. Wilson, 1971: Correlation of Winds and Geographic Features with Production of Certain Infrasonic Signals in the Atmosphere. – Geophys. J. Int. **26**, 201–214, DOI: 10.1111/j.1365-246X.1971.tb03395.x.

Le Pichon, A., E. Blanc, D. Drob, S. Lambotte, J.X. Dessa, M. Lardy, P. Bani, S. Vergniolle, 2005: Infrasound monitoring of volcanoes to probe high-altitude winds. – J. Geophys. Res. **110**, D13106, DOI: 10.1029/2004JD005587.

Le Pichon, A., J. Vergoz, P. Herry, L. Ceranna, 2008: Analyzing the detection capability of infrasound arrays in Central Europe. – J. Geophys. Res. **113**, D12115, DOI: 10.1029/2007JD009509.

Le Pichon, A., R. Matoza, N. Brachet, Y. Cansi, 2010: Recent Enhancements of the PMCC Infrasound Signal Detector. – Inframatics **26**, 5–8.

Le Pichon, A., L. Ceranna, J. Vergoz, 2012: Incorporating numerical modeling into estimates of the detection capability of the IMS infrasound network. – J. Geophys. Res. **117**, D05121, DOI: 10.1029/2011JD016670.

Le Pichon, A., L. Ceranna, C. Pilger, P. Mialle, D. Brown, P. Herry, N. Brachet, 2013: The 2013 Russian fireball largest ever detected by CTBTO infrasound sensors. – Geophys. Res. Lett. **40**, 3732–3737, DOI: 10.1002/grl.50619.

Le Pichon, A., L. Ceranna, J. Vergoz, D. Tailpied, 2019: Modeling the Detection Capability of the Global IMS Infrasound Network. – In: A. Le Pichon, E. Blanc, A. Hauchecorne (Eds.): Infrasound Monitoring for Atmospheric Studies – Challenges in Middle-atmosphere Dynamics and Societal Benefits, 593–604. Springer, Dordrecht, the Netherlands, DOI: 10.1007/978-3-319-75140-5_17.

Leutbecher, M., H. Volkert, 2000: The Propagation of Mountain Waves into the Stratosphere: Quantitative Evaluation of Three-Dimensional Simulations. – J. Atmos. Sci. **57**, 3090–3108, DOI: 10.1175/1520-0469(2000)057<3090:TPOMWI>2.0.CO;2.

Limpasuvan, V., D.L. Wu, M.J. Alexander, M. Xue, M. Hu, S. Pawson, J.R. Perkins, 2007: Stratospheric gravity wave simulation over Greenland during 24 January 2005. – J. Geophys. Res. **112**, D10115, DOI: 10.1029/2006jd007823.

Lingevitch, J.F., M.D. Collins, D.K. Dacol, D.P. Drob, J.C.W. Rogers, W.L. Siegmann, 2002: A wide angle and high Mach number parabolic equation. – J. Acoust. Soc. Am. **111**, 729–734, DOI: 10.1121/1.1430683.

Lund, T., D. Fritts, B. Laughman, H. Liu, 2018: High-resolution numerical simulation of breaking gravity waves due to winds over the southern Andes mountains. – In: EGU General Assembly, volume 20, EGU2018-11761.

Margrave, G.F., 2000: New seismic modelling facilities in Matlab. Research Report 12, Consortium for Research in Elastic Wave Exploration Seismology (CREWES), University of Calgary, Alberta, Canada last accessed: 27 October 2018.

Matoza, R.S., D. Fee, 2018: The Inaudible Rumble of Volcanic Eruptions. – Acoustics Today **14**, 17–25.

Matoza, R.S., M. Landès, A. Le Pichon, L. Ceranna, D. Brown, 2013: Coherent ambient infrasound recorded by the International Monitoring System. – Geophys. Res. Lett. **40**, 429–433, DOI: 10.1029/2012GL054329.

McLandress, C., M.J. Alexander, D.L. Wu, 2000: Microwave Limb Sounder observations of gravity waves in the stratosphere: A climatology and interpretation. – J. Geophys. Res. **105**, 11947–11967, DOI: 10.1029/2000JD900097.

Meecham, W.C., 1971: On aerodynamic infrasound. – J. Atmos. Terr. Phys. **33**, 149–155, DOI: 10.1016/0021-9169(71)90193-0.

Nappo, C.J., 2012: An Introduction to Atmospheric Gravity Waves, volume 102 of International Geophysics. – Academic Press, San Diego, CA, USA, 400.

Nishida, K., Y. Fukao, S. Watada, N. Kobayashi, M. Tahira, N. Suda, K. Nawa, T. Oi, T. Kitajima, 2005: Array observation of background atmospheric waves in the seismic band from 1 mHz to 0.5 Hz. – Geophys. J. Int. **162**, 824–840, DOI: 10.1111/j.1365-246X.2005.02677.x.

Norris, D., R. Gibson, K. Bongiovanni, 2010: Numerical Methods to Model Infrasonic Propagation Through Realistic Specifications of the Atmosphere. – In: A. Le Pichon, E. Blanc, A. Hauchecorne (Eds.): Infrasound Monitoring for Atmospheric Studies, 541–573. Springer, Dordrecht, the Netherlands, DOI: 10.1007/978-1-4020-9508-5_17.

Picone, J.M., A.E. Hedin, D.P. Drob, A.C. Aikin, 2002: NRLMSISE-00 empirical model of the atmosphere: Statistical comparisons and scientific issues. – J. Geophys. Res. **107**, A121468, DOI: 10.1029/2002ja009430.

Pilger, C., L. Ceranna, J.O. Ross, A. Le Pichon, P. Mialle, M.A. Garcés, 2015: CTBT infrasound network performance to detect the 2013 Russian fireball event. – Geophys. Res. Lett. **42**, 2523–2531, DOI: 10.1002/2015GL063482.

Pilger, C., L. Ceranna, J.O. Ross, J. Vergoz, A. Le Pichon, N. Brachet, E. Blanc, J. Kero, L. Liszka, S. Gibbons, T. Kvaerna, S.P. Näsholm, E. Marchetti, M. Ripepe, P. Smets, L. Evers, D. Ghica, C. Ionescu, T. Sindelarova, Y. Ben Horin, P. Mialle, 2018: The European Infrasound Bulletin. – Pure Appl. Geophys., DOI: 10.1007/s00024-018-1900-3.

Rapp, M., A. Dörnbrack, B. Kaifler, 2018: An intercomparison of stratospheric gravity wave potential energy densities from METOP GPS radio occultation measurements and ECMWF model data. – Atmos. Meas. Tech. **11**, 1031–1048, DOI: 10.5194/amt-11-1031-2018.

Rockway, J.W., G.L. Hower, L.B. Craine, J.E. Thomas, 1974: Applications of Ray-Tracing to Observations of Mountain-Associated Infrasonic Waves. – Geophys. J.R. Astron. Soc. **36**, 259–266, DOI: 10.1111/j.1365-246X.1974.tb03637.x.

Sabatini, R., J.B. Snively, C. Bailly, M.P. Hickey, J.L. Garrison, 2019: Numerical Modeling of the Propagation of Infrasonic Acoustic Waves Through the Turbulent Field Generated by the Breaking of Mountain Gravity Waves. – Geophys. Res. Lett. **46**, DOI: 10.1029/2019GL082456.

Shevov, N.N., A.I. Semenov, N.N. Pertsev, V.A. Sukhodoev, 2000: The Spatial Distribution of Gravity Wave Energy Influx Into the Mesopause Over a Mountain Lee. – Phys. Chem. Earth (B) **25**, 541–545.

Sutherland, L.C., H.E. Bass, 2004: Atmospheric absorption in the atmosphere up to 160 km. – J. Acoust. Soc. Am. **115**, 1012–1032, DOI: 10.1121/1.1631937.

Thomas, J.E., T.H. Kuckertz, J.D. Logan, T.K. Law, L.B. Craine, 1974: Possible source mechanisms for a frequently occurring infrasonic signal. – J. Acoust. Soc. Amer. **56**, 1391–1397, DOI: 10.1121/1.1903456.

Wilson, D.K., 2003: The sound-speed gradient and refraction in the near-ground atmosphere. – J. Acoust. Soc. Amer. **113**, 750–757, DOI: 10.1121/1.1532028.

Wilson, C.R., C.A.L. Szuberla, J.V. Olson, 2010: High-latitude Observations of Infrasound from Alaska and Antarctica: Mountain-Associated Waves and Geomagnetic/Auroral Infrasonic Signals. – In: A. Le Pichon, E. Blanc, and A. Hauchecorne (Eds.): Infrasound Monitoring for Atmospheric Studies, 415–454. Springer, Dordrecht, the Netherlands, DOI: 10.1007/978-1-4020-9508-5_13.

Zeng, X., X. Xue, X. Dou, C. Liang, M. Jia, 2017: COSMIC GPS observations of topographic gravity waves in the stratosphere around the Tibetan Plateau. – Science China – Earth Sciences **60**, 188–197, DOI: 10.1007/s11430-016-0065-6.

The pdf version (Adobe Java Script must be enabled) of this paper includes an electronic supplement:
Table of content – Electronic Supplementary Material (ESM)

Figures S1, S2, S3